

AD/A-006 690

EFFECTS OF AIRPLANE FLOW FIELDS ON
HYDROMETEOR CONCENTRATION
MEASUREMENTS

Hillyer G. Norment, et al

Mount Auburn Research Associates, Incorporated

Prepared for:

Air Force Cambridge Research Laboratories

6 December 1974

DISTRIBUTED BY:

NTIS

National Technical Information Service
U. S. DEPARTMENT OF COMMERCE

UNCLASSIFIED

SECURITY CLASSIFICATION OF THIS PAGE (When Data Entered)

REPORT DOCUMENTATION PAGE		READ INSTRUCTIONS BEFORE COMPLETING FORM
1. REPORT NUMBER AFCRL - TR - 74 - 0602	2. GOVT ACCESSION NO.	3. RECIPIENT'S CATALOG NUMBER <i>AD/A006690</i>
4. TITLE (and Subtitle) EFFECTS OF AIRPLANE FLOW FIELDS ON HYDROMETEOR CONCENTRATION MEASUREMENTS		5. TYPE OF REPORT & PERIOD COVERED Scientific - Final 7/1/73 - 11/30/74
		6. PERFORMING ORG. REPORT NUMBER
7. AUTHOR(s) Hillyer G. Norment Robert G. Zalosh		8. CONTRACT OR GRANT NUMBER(s) F19628-73-C-0114
9. PERFORMING ORGANIZATION NAME AND ADDRESS Mt. Auburn Research Associates, Inc. 385 Elliot Street Newton, Massachusetts 02164		10. PROGRAM ELEMENT, PROJECT, TASK AREA & WORK UNIT NUMBERS 7605-04-01 63311F
11. CONTROLLING OFFICE NAME AND ADDRESS Air Force Cambridge Research Laboratories (LYC) Hanscom Field, Massachusetts 01731 Contract Monitor: Mr. Morton Glass		12. REPORT DATE 6 December 1974
14. MONITORING AGENCY NAME & ADDRESS (if different from Controlling Office)		13. NUMBER OF PAGES 112 / 108
		15. SECURITY CLASS. (of this report) Unclassified
16. DISTRIBUTION STATEMENT (of this Report) Approved for public release; distribution unlimited		
17. DISTRIBUTION STATEMENT (of the abstract entered in Block 20, if different from Report)		
18. SUPPLEMENTARY NOTES		
19. KEY WORDS (Continue on reverse side if necessary and identify by block number) cloud physics Lockheed C130A, C130E water drop concentration large particle trajectory calculation ice column concentration meteorological research airplanes concentration factor effect of airflow on particle concentration Cessna Citation calibration of airborne hydrometeor samplers		
20. ABSTRACT (Continue on reverse side if necessary and identify by block number) A method is described by which concentration distortion of particulates of arbitrary sizes caused by airflow around airplane fuselages can be calculated. The method accounts for effects of: three-dimensional details of the fuselage shape on airflow, angle-of-attack on airflow, altitude, interaction of the particles with the airflow, and particle settling. It has been applied to hydrometeor sampling instruments on three cloud physics airplanes: Lockheed C130A and C130E transports, and a Cessna Citation jet.		

DD FORM 1473

1 JAN 73

EDITION OF 1 NOV 65 IS OBSOLETE

UNCLASSIFIED

(continued)

SECURITY CLASSIFICATION OF THIS PAGE (When Data Entered)

Reproduced by
NATIONAL TECHNICAL
INFORMATION SERVICE
US Department of Commerce
Springfield, VA. 22151

UNCLASSIFIED

SECURITY CLASSIFICATION OF THIS PAGE(When Data Entered)

Detailed results for water drops and ice columns are presented. In all cases very substantial concentration enhancement is indicated over broad ranges of particle sizes. Several of the instrument sampling points are found to lie in "shadow zones", wherein particles of certain sizes cannot be sampled. An accuracy analysis indicates that, at least for water drops, the method can be used to correct existing data.

UNCLASSIFIED

SECURITY CLASSIFICATION OF THIS PAGE(When Data Entered)

PREFACE

This study is a part of the Advanced Ballistics Reentry Systems (ABRES) program, a major concern of which is to estimate nose cone erosion by water and ice particles in natural clouds.

The authors acknowledge with gratitude the support and guidance of Dr. Robert Cunningham and Mr. Morton Glass of the Convective Cloud Physics Branch, AFCRL.

TABLE OF CONTENTS

	<u>Page</u>
INTRODUCTION	1
NATURE OF THE PROBLEM	5
THEORY	10
Concentration Factor	10
Particle Trajectory Calculation	16
Three-dimensional Flow Calculation	20
HYDROMETEOR TYPES	24
Water Drops	24
Ice Crystals	24
RESULTS	30
Particle Replicator on the Lockheed C130A	30
Particle Replicator on the Lockheed C130E	44
Knollenberg Particle Spectrometers on the Cessna Citation	52
ACCURACY OF THE METHOD	66
Numerical Integration	66
Potential Flow Calculations	68
Aerodynamic Particle Drag	69
Sensitivity to Flux Tube Structure	74
Particle Shape and Orientation	74
Summary and Discussion	76
CONCLUSIONS	77
APPENDIX A. ITERATIVE PROCEDURES TO DETERMINE THE PARTICLE TRAJECTORY THROUGH A POINT IN SPACE	79
APPENDIX B. AERODYNAMIC DRAG ON MOVING PARTICLES	83
General Considerations	83
Spheres	84
Columns	87
Application of the Drag Polynomials	91
APPENDIX C. PROJECTED DIMENSION OF RANDOMLY ORIENTED RECTANGLES	93
APPENDIX D. GLOSSARY OF SYMBOLS	95
REFERENCES	99

LIST OF FIGURES

<u>Figure Number</u>		<u>Page</u>
1	Lockheed C130A Transport outfitted for cloud physics studies.	2
2	Cessna Citation Executive Jet.	3
3	Axisymmetric potential flow streamlines about a prolate ellipsoid of fineness ratio 2	6
4	Trajectories of 50 μm diameter water drops in potential airflow about a prolate ellipsoid of fineness ratio 2	7
5	Trajectories of 100 μm diameter water drops in potential airflow about a prolate ellipsoid of fineness ratio 2	8
6	Trajectories of 100 μm diameter water drops in potential airflow about a prolate ellipsoid of fineness ratio 2	9
7	Perspective view of a particle flux tube	12
8	Target and initial plane flux tube cross sections for 50 μm water drops passing through the C130A particle replicator slit	14
9	Computer prepared plot of the digital description of the nose and cabin sections of the Lockheed C130A airplane	22
10	Properties of hexagonal-based plates and columns	26
11	Lockheed C130A with formvar replicator arm in position	31
12	Computer prepared plot of the digital description of the complete Lockheed C130A fuselage	32
13	Water drop concentration factors at and near the particle replicator slit on the Lockheed C130A	34

<u>Figure Number</u>		<u>Page</u>
14a,b	Stereographic plots of 20 and 100 μm water drop flux tubes to the Lockheed C130A particle replicator slit.	36,37
15	Concentration factor vs. particle mass for solid ice columns at the particle replicator slit on the Lockheed C130A.	38
16	Concentration factor vs. particle mass for hollow ice columns at the particle replicator slit on the Lockheed C130A	39
17	Concentration factor vs. mean projected column dimension for solid ice columns at the particle replicator slit on the Lockheed C130A.	40
18	Concentration factor vs. mean projected dimension for hollow ice columns at the particle replicator slit on the Lockheed C130A.	41
19	Particle replicator arm geometry on the Lockheed C130E	45
20	Computer prepared plot of the digital description of the Lockheed C130E forward fuselage to FS 350"	46
21	Computer prepared plot of the digital description of the complete Lockheed C130E fuselage	47
22	Concentration factor contours vs. water drop diameter along the particle replicator arm on the Lockheed C130E	48
23a,b	Stereographic plots of a six-trajectory, 150 μm diameter flux tube to a point 10 cm outboard from the Lockheed C130E particle replicator slit.	49,50
24	Cloud physics instrumentation mounted on the Cessna Citation	53
25	Computer-prepared plot of the digital description of the forward fuselage of the Cessna Citation	54
26	Computer-prepared plot of the complete Cessna Citation fuselage description	55

<u>Figure Number</u>		<u>Page</u>
27	Concentration factors vs. water drop diameters for the Knollenberg particle spectrometers on the Cessna Citation	57
28	Concentration factor vs. particle mass for solid and hollow ice columns at the precipitation particle spectrometer on the Cessna Citation	59
29	Concentration factor vs. particle mass for solid and hollow ice columns at the cloud particle spectrometer on the Cessna Citation	60
30	Concentration factor vs. mean projected column dimension for solid and hollow ice columns at the precipitation particle spectrometer on the Cessna Citation	61
31	Concentration factor vs. mean projected column dimension for solid and hollow ice columns at the cloud particle spectrometer on the Cessna Citation	62
32a,b	Stereographic plots of four-trajectory, 150 μ m diameter water drop flux tubes to the Cessna Citation cloud particle spectrometer and precipitation particle spectrometer	64,65
33	Comparison of water drop trajectories about an ellipsoid of fineness ratio 2 using exact and approximate potential airflow	70
34	Relaxation times of water drops, computed by steady-state and Ingebo drag coefficients, in response to a 1 m/sec impulsive horizontal flow	73
C.1	Geometry of a rectangle oriented at angle θ to the projection direction	94

LIST OF TABLES

<u>Table Number</u>		<u>Page</u>
1	AIRPLANE FLIGHT CONDITIONS	4
2	RATIO OF AIRSPEED AT SAMPLING POINTS TO FREE- STREAM AIRSPEED	11
3	COLUMNAR CRYSTAL PROPERTIES	29
4	WATER DROP CONCENTRATION FACTORS AT AND NEAR THE REPLICATOR SLIT ON THE LOCKHEED C130A	35
5	ICE COLUMN CONCENTRATION FACTORS AT THE PARTICLE REPLICATOR SLIT ON THE LOCKHEED C130A (AXIS-ON DRAG)	42
6.	ICE COLUMN CONCENTRATION FACTORS AT THE PARTICLE REPLICATOR SLIT ON THE LOCKHEED C130A (END-ON DRAG)	43
7	WATER DROP CONCENTRATION FACTORS FOR THE REPLICATOR ON THE LOCKHEED C130E	51
8	WATER DROP CONCENTRATION FACTORS FOR THE PARTICLE SPECTROMETERS ON THE CESSNA CITATION	58
9	CONCENTRATION FACTORS FOR ICE COLUMNS AT THE KNOLLENBERG SPECTROMETERS ON THE CESSNA CITATION	63
10	COMPARISON OF TANGENT TRAJECTORY RESULTS WITH THOSE OF DORSCH ET AL.	68
11	COMPARISON OF STEADY-STATE AND INGEBO DRAG CONCENTRATION FACTORS AT THE PARTICLE REPLICATOR ON THE LOCKHEED C130A	72
12	SENSITIVITY OF C_F TO FLUX TUBE STRUCTURE	75
13	POLYNOMIAL COEFFICIENTS RELATING BEST NUMBER TO REYNOLDS NUMBER FOR SPHERES	86
14	POLYNOMIAL COEFFICIENTS RELATING REYNOLDS NUMBER TO BEST NUMBER FOR AXIS-ON TERMINAL SETTLING OF CYLINDERS	88

Table
Number

Page

15 POLYNOMIAL COEFFICIENTS RELATING BEST NUMBER
 TO REYNOLDS NUMBER FOR AXIS-ON CYLINDER DRAG

89

16 POLYNOMIAL COEFFICIENTS RELATING BEST NUMBER
 TO REYNOLDS NUMBER FOR END-ON CYLINDER DRAG

90

INTRODUCTION

It is current practice in cloud physics research to make in situ measurements of hydrometeors via instrumented low speed airplanes. Quantitative estimates of hydrometeor concentrations and size spectra are obtained with particle replicators^(1,2) and Knollenberg particle spectrometers⁽³⁾. Ideally, these instruments are mounted such that measurements are made (or samples taken) in the undisturbed free-stream, thereby avoiding concentration distortion caused by airflow about the airplane. However, because of competition for the best locations and the many problems with remote control of instruments, ideal mounting is frequently not possible. Then it is necessary to make rational choices between the various options available, and if possible, to correct observed data to remove distortions. A method that has proved successful in accomplishing both of these goals is described herein.

The method has been applied to instrumentation on three airplanes: Lockheed C130A and C130E transports, and a Cessna Citation executive jet. The Lockheed airplanes (Fig. 1), which are similar in appearance except for a longer nose radome on the C130E, are instrumented for use by the Convective Cloud Physics Branch, Cambridge Research Laboratories. We have done extensive theoretical studies of formvar particle replicators mounted on these airplanes. The Cessna airplane (Fig. 2) has been instrumented for cloud physics studies by Meteorology Research, Inc. We have studied Knollenberg particle spectrometers mounted on this airplane. Flight conditions for the three airplanes are given in Table 1.

-
1. P. Spyers-Duran and R. R. Braham, "An Airborne Continuous Cloud Particle Replicator," J. Appl. Meteor. 6, 1108 (1967).
 2. J. Hallett, R. W. Hanaway, and P. B. Wagner, "Design and Construction of a New Cloud Particle Replicator for Use on a Pressurized Aircraft," Desert Research Institute, Reno, Nevada, AFCRL-72-0410 (31 May 1972). AD-753 091.
 3. R. G. Knollenberg, "The Optical Array: An Alternative to Scattering or Extinction for Airborne Particle Size Determination," J. Appl. Meteor. 9, 86 (1970).

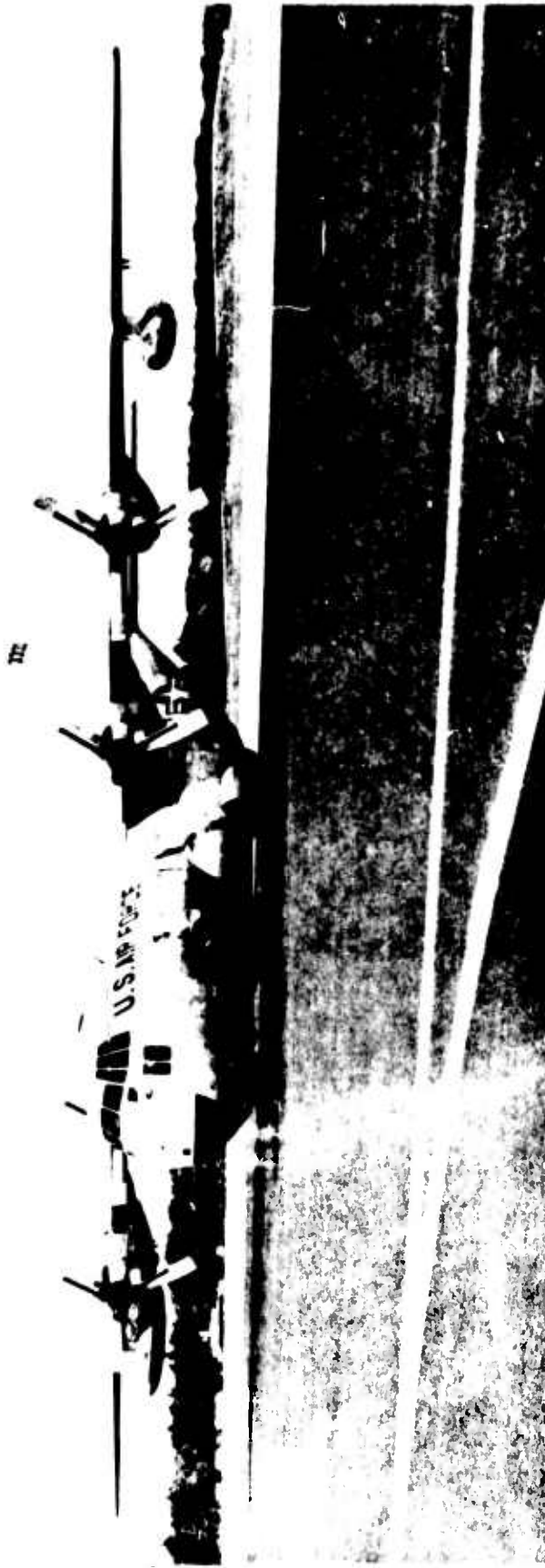


FIGURE 1. Lockheed C130A transport outfitted for cloud physics studies. Wingspan - 132 feet; overall length - 95 feet; fuselage radius - 85 inches. Locations of the particle replicators are shown in Figs. 9 and 20.

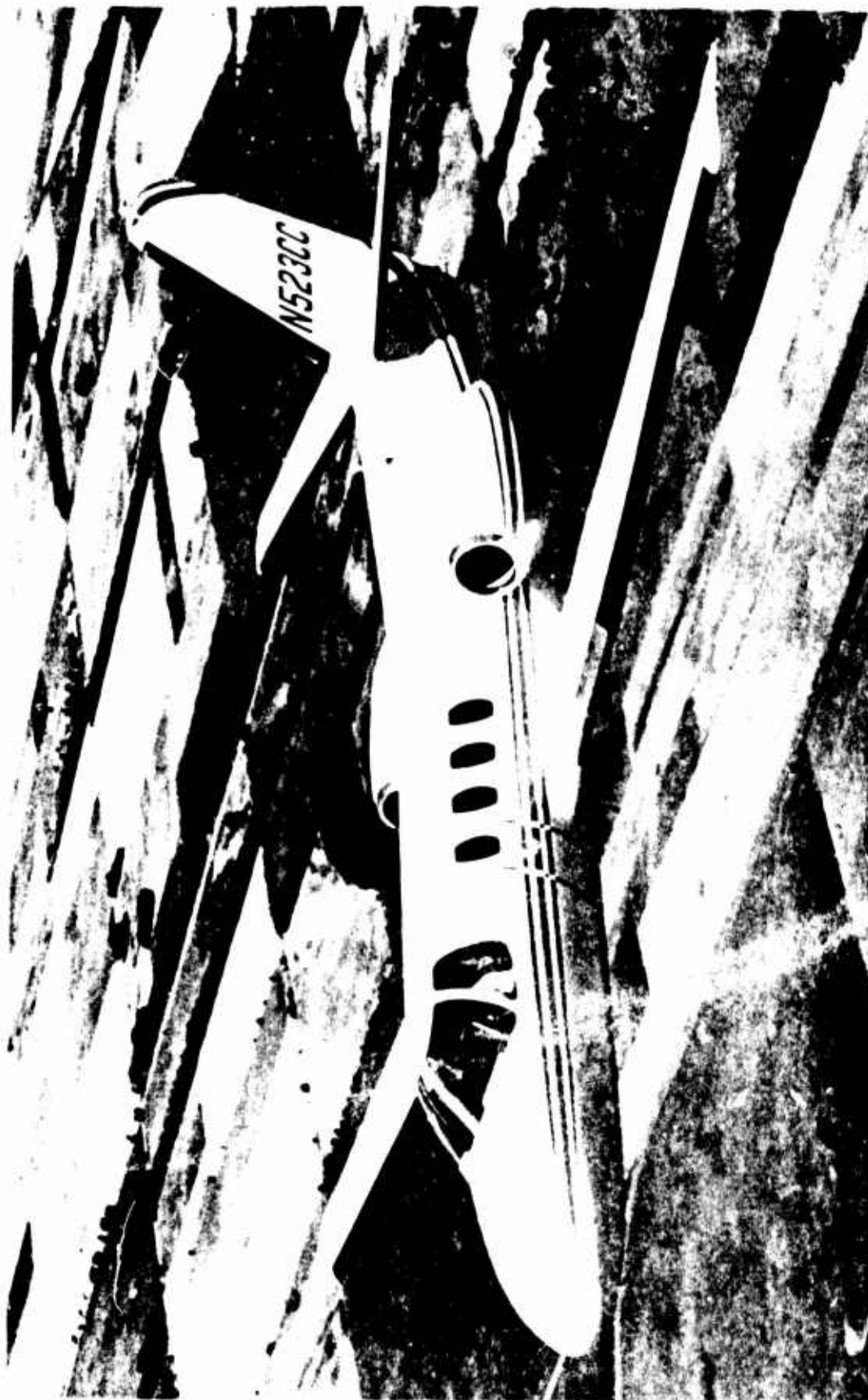


FIGURE 2. Cessna Citation Executive Jet. Wingspan - 44 feet; overall length - 44 feet; fuselage radius - 265 feet. Location of the Knollenberg spectrometers is shown in Fig. 25.

TABLE 1

AIRPLANE FLIGHT CONDITIONS

<u>Airplane</u>	<u>Indicated airspeed (kts)</u>	<u>Angle- of- attack (deg)</u>	<u>Altitude (kft)</u>	<u>True airspeed (kts)</u>	<u>Temperature (°K)</u>	<u>Air density (kg/m³)</u>	<u>Air viscosity (kg/(m-sec))</u>
Lockheed C130A	162	4°	5	177.6	278.3	1.055	1.741×10^{-5}
	162	4°	30	265.1	229.5	0.459	1.491×10^{-5}
Lockheed C130E	162	4°	5	177.6	278.3	1.055	1.741×10^{-5}
Cessna Citation	120	3°	20	167.2	248.6	0.653	1.592×10^{-5}

NATURE OF THE PROBLEM

Consider axisymmetric airflow about a prolate ellipsoid (Fig. 3), which we can use as a simple approximation to an aircraft fuselage. If a particle sampling instrument were positioned near the fuselage, for example at the point marked \otimes in Fig. 3, and if the particles were to follow the stream flow, then from the streamline spacing contraction it is apparent that a higher particle flux would be measured than exists in the free-stream. This could be evaluated by straightforward analysis of the flow.

The situation is more complicated when the inertia of the particles causes them to deviate from the streamlines. Inertia effects are illustrated by Figs. 4, 5, and 6, which show computed water drop trajectories for drops of 50, 100, and 1000 μm diameter, respectively, in the potential flow field of Fig. 3. In Fig. 4 the trajectories closest to the ellipsoid are seen to deflect outward. In Fig. 5 there is both impaction on the ellipsoid and substantial trajectory deflection. These effects conspire to produce quite high particle fluxes at, for example, point 1 in Fig. 5, whereas at point 2 we should not expect to sample water drops of this size. Point 2 lies in a "shadow zone" region, and adjacent to this region we expect high particle concentrations and very steep concentration gradients. (Characteristically, we find maximum concentration distortion for water drops of about 100 μm diameter.) For Fig. 6 we see that considerably larger water drops possess sufficient inertia that they substantially ignore airflow about the ellipsoid.

Notice the left-to-right downward slant of the trajectories in Fig. 6. This is caused by gravity settling of the drops. Thus, though the airflow is axisymmetric, the particle flux is not. Moreover, bodies of revolution are poor approximations to fuselages, wings, etc., and angle-of-attack departures from axisymmetric flow need to be accounted for. Clearly three-dimensional methods are required.

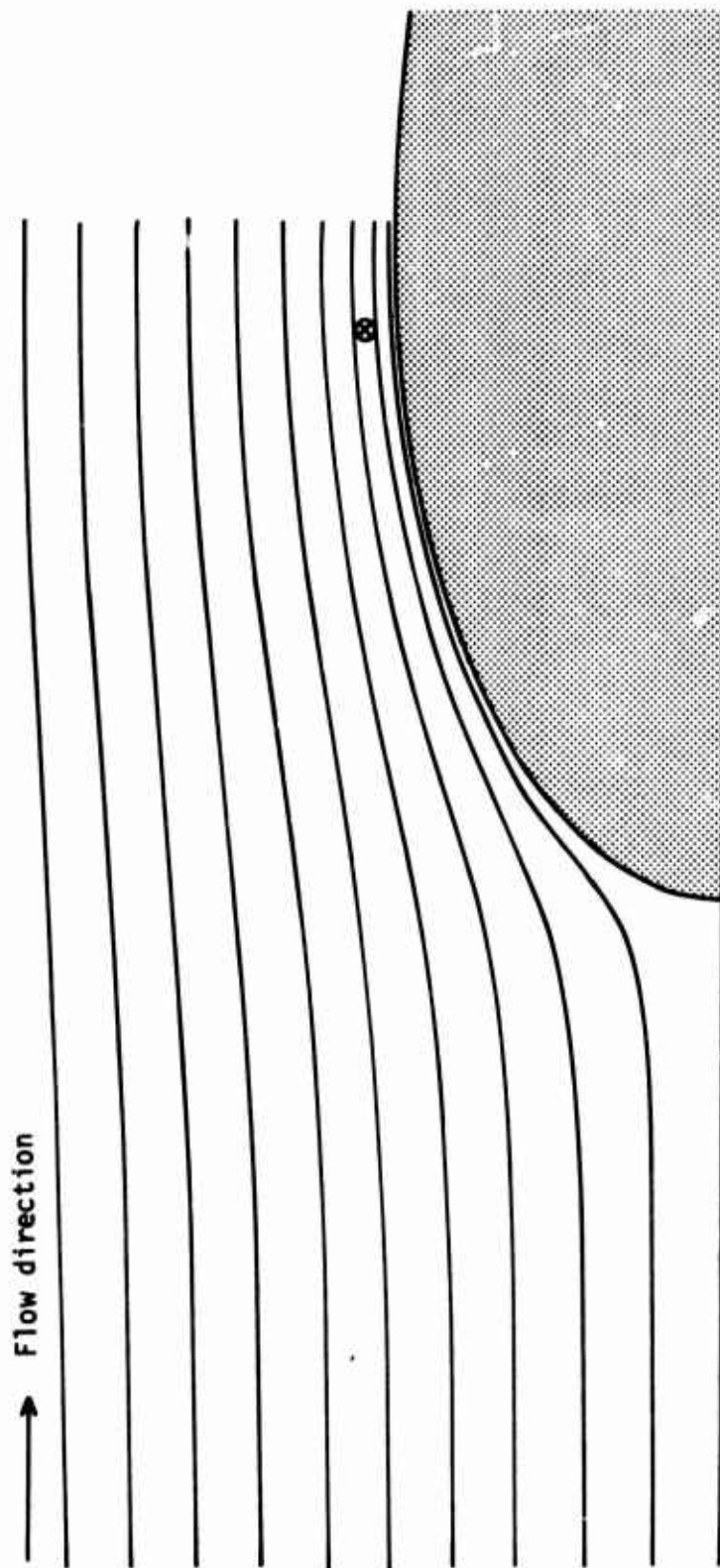


FIGURE 3. Axisymmetric potential flow streamlines about a prolate ellipsoid of fineness ratio 2.

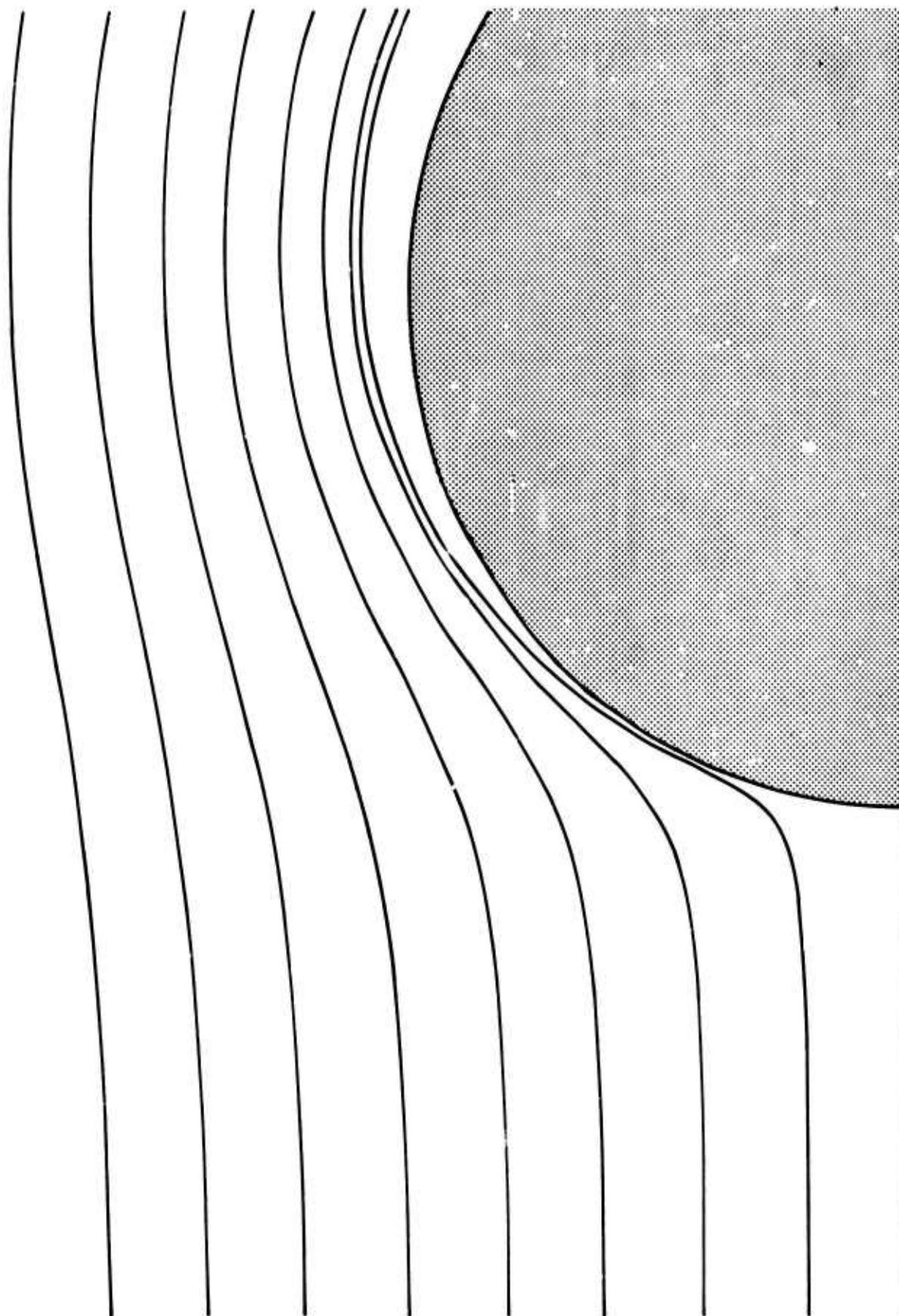


FIGURE 4. Trajectories of 50 μm diameter water drops in potential airflow about a prolate ellipsoid of fineness ratio 2. (The ordinate scale is expanded by a factor of 2.)

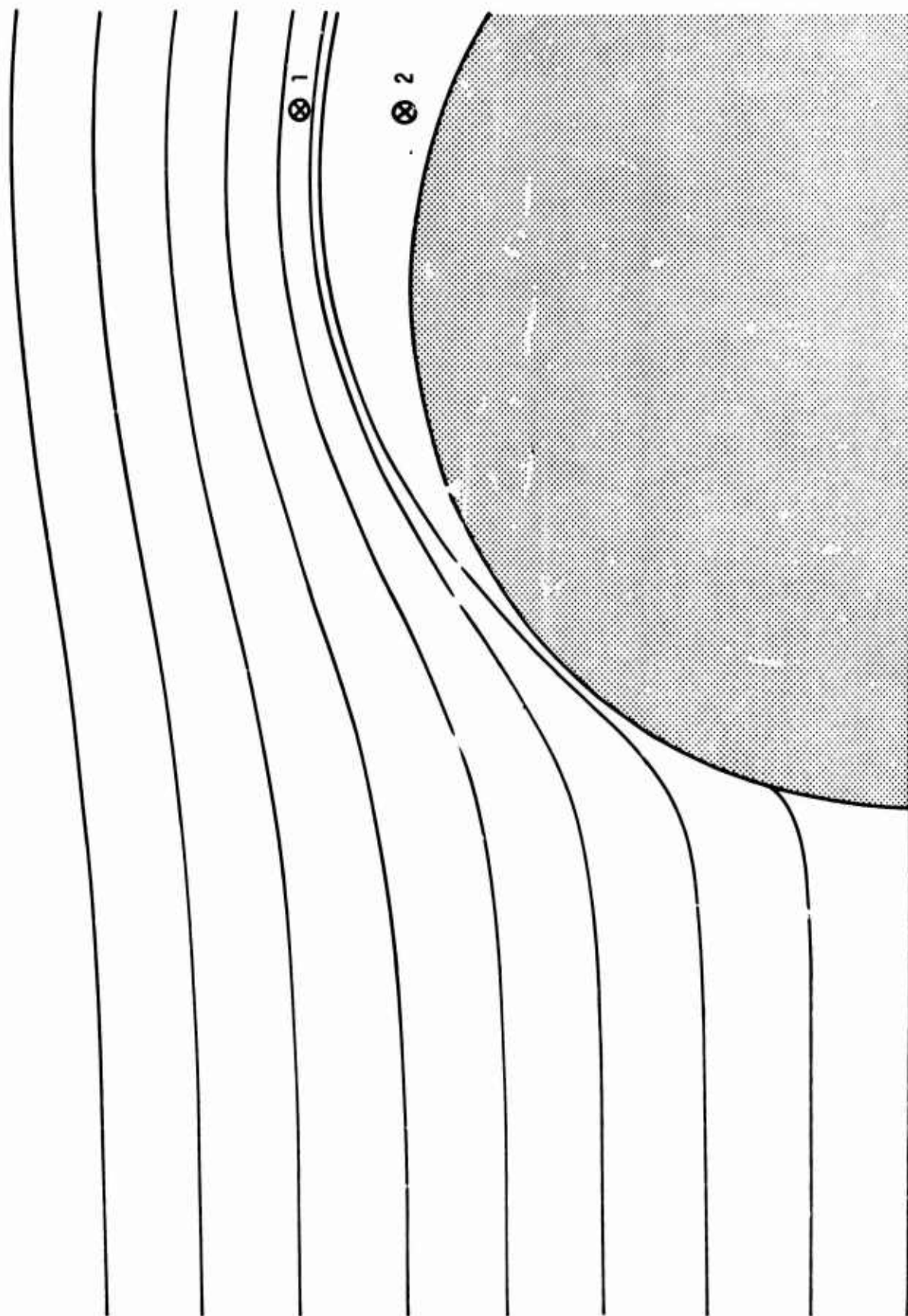


FIGURE 5. Trajectories of 100 μm diameter water drops in potential airflow about a prolate ellipsoid of fineness ratio 2. (The ordinate scale is expanded by a factor of 2.)

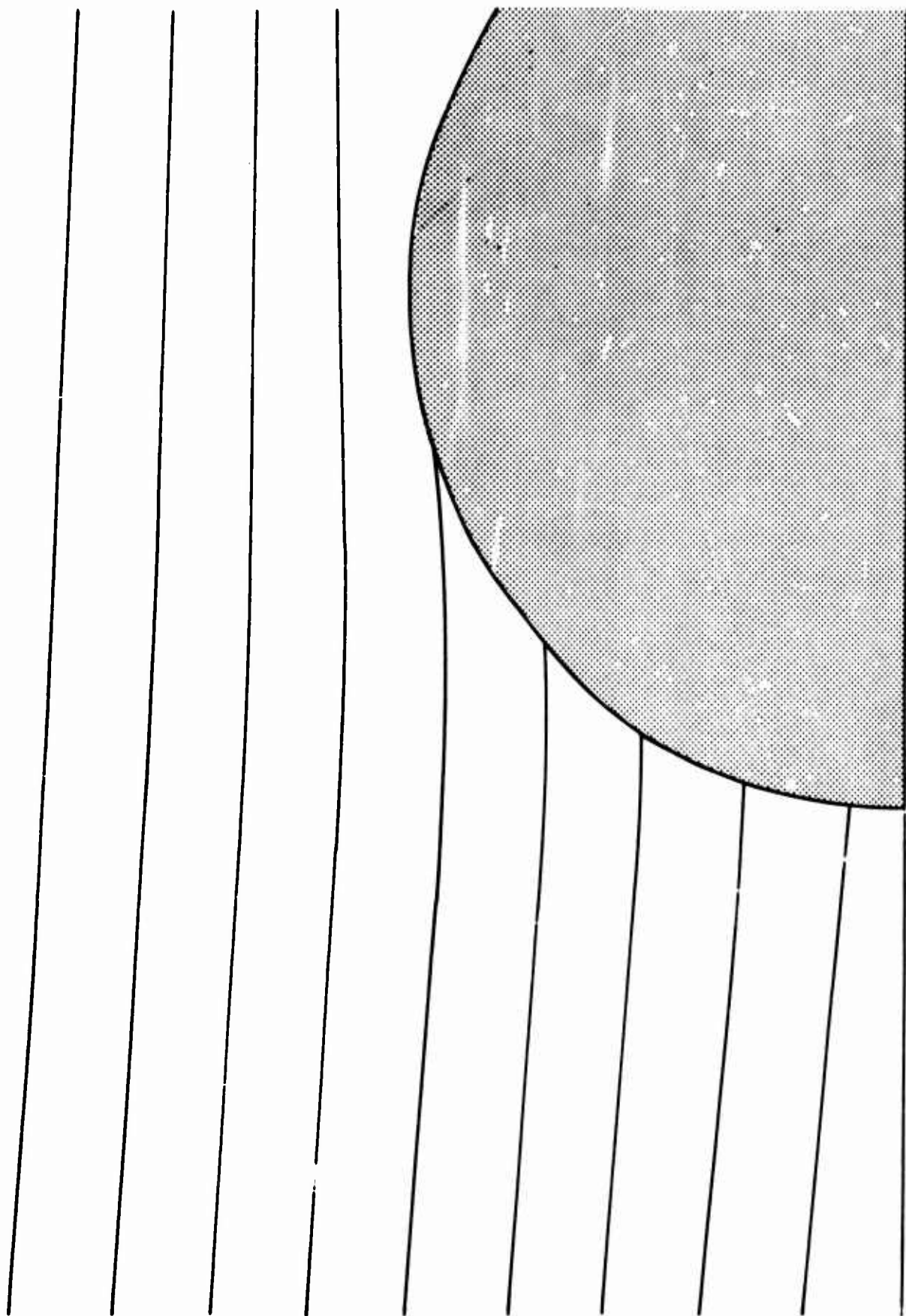


FIGURE 6. Trajectories of 1000 μm diameter water drops in potential airflow about a prolate ellipsoid of fineness ratio 2. (The ordinate scale is expanded by a factor of 2.)

THEORY

CONCENTRATION FACTOR

Principal results of this work are expressed in a quantity called concentration factor. Concentration factor, C_F is defined⁽⁴⁾ as the ratio of particle flux (i.e., mass of particles passing per second through a unit area normal to the particle velocity) at the sampling or target point, F_t , to the particle flux in the free-stream, F ,

$$C_F \equiv \frac{F_t}{F} \quad . \quad (1)$$

The ratio of particle concentration at the target point to free-stream concentration, C_M , is

$$C_M \approx C_F V/V_t \quad , \quad (2)$$

where V is free-stream airspeed and V_t is airspeed at the target point. In this latter definition we ignore difference between particle and air velocities. Since $V_t/V \approx 1$ (within 10% for all cases studied, see Table 2) we confine our attention hereafter to the more precise quantity C_F .

In three dimensions we determine concentration factor via calculation of a particle flux tube (Fig. 7). This tube, which is analogous to a streamtube, is determined such that there is no particle flux through its boundaries; therefore mass transfer of particles is equal through all cross-sections. It is centered about a central trajectory (the heavy dashed curve in Fig. 7) that passes through the primary target point. The initial and target planes are perpendicular to the central trajectory.

4. R. G. Dorsch and R. J. Brun, "Variation of Local Liquid-Water Concentration About an Ellipsoid of Finesness Ratio 5 Moving in a Droplet Field," NACA-TN-3153 (July 1954).

TABLE 2

RATIO OF AIRSPEED AT SAMPLING POINTS TO FREE-STREAM AIRSPEED

<u>Airplane</u>	<u>Instrument</u>	<u>Altitude (kft)</u>	<u>v_t</u>
Lockheed C130A	Particle replicator	5	1.102
	Particle replicator	30	1.102
Lockheed C130E	Particle replicator	5	1.040
Cessna Citation	Precipitator particle spectrometer	20	1.017
	Cloud particle spectrometer	20	1.020

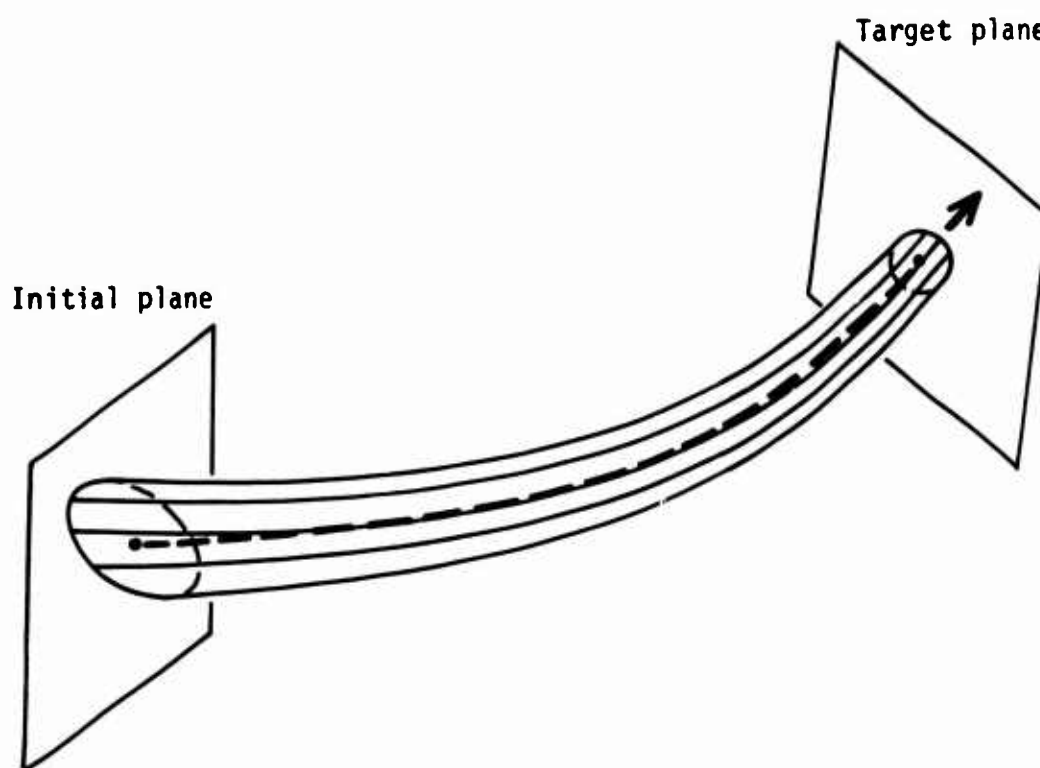


FIGURE 7. Perspective view of a particle flux tube

If \dot{M} is the particle mass transfer rate through the tube, then at any point along the tube

$$\dot{M} = FA, \quad (3)$$

where A is the perpendicular cross section area of the tube. Since \dot{M} is constant in a particle flux tube,

$$C_F \approx \frac{A}{A_t}, \quad (4)$$

or

$$C_F = \lim_{\substack{A \rightarrow 0 \\ A_t \rightarrow 0}} \left(\frac{A}{A_t} \right), \quad (5)$$

where A and A_t are the cross-sectional areas of the flux tube in the free-stream and at the target point, respectively.

In broad outline, our procedure is as follows. We define a circular "window" (i.e. flux tube surface trace) in the target plane. Our primary target point is at the center of this circle. A number of evenly spaced points (usually 6 or 8) are chosen on the window circumference. Then, by use of an iterative procedure, described below and in Appendix A, we establish the particle trajectories that pass through these points. We take the trajectory intersection points with the target and initial planes to be the vertices of plane polygons: an approximate regular polygon in the target plane, and an irregular (distorted) polygon in the initial plane (Fig. 8). We compute the areas of these polygons, and take the concentration factor to be the ratio of these areas.

Owing to the geometrical connection between stream tube cross-sections in the initial and target planes, we hypothesize that they can be related via a conformal mapping transformation. Let a complex point

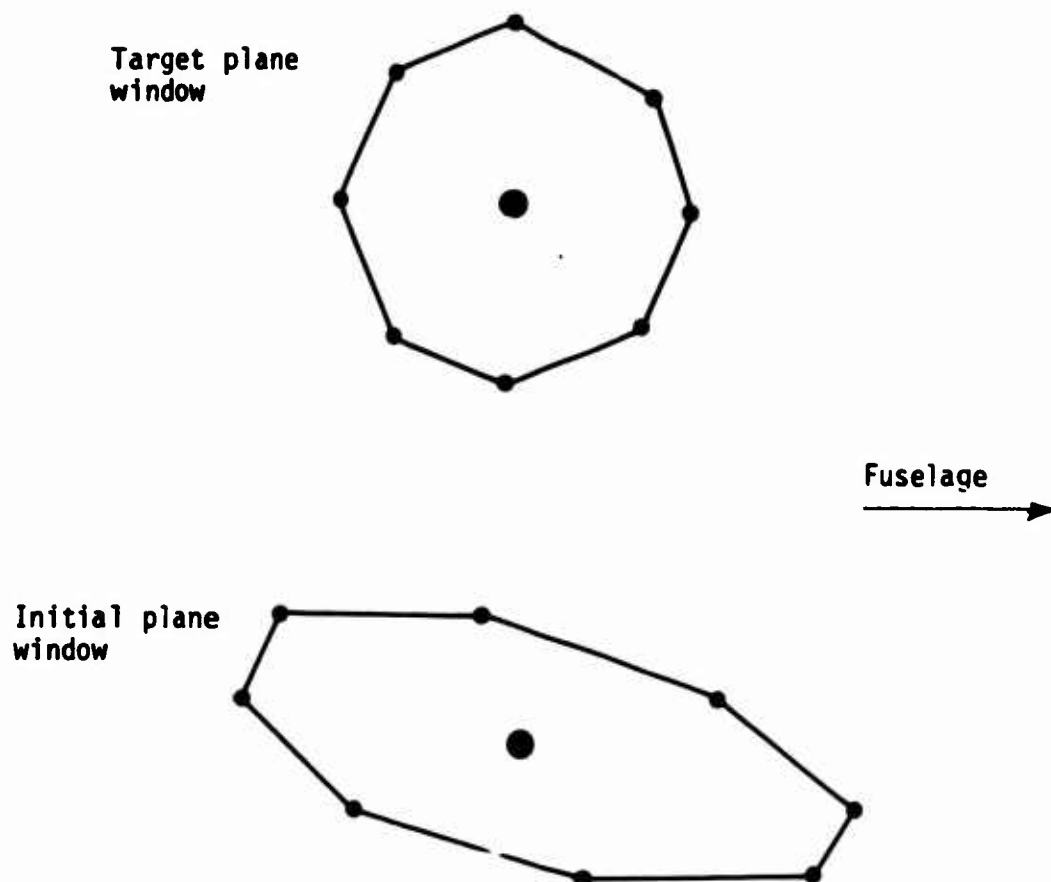


FIGURE 8. Target and initial plane flux tube cross sections for 50 μm water drops passing through the C130A particle replicator slit.
 $C_F = 1.271$, $r_w = 0.02$, $\epsilon = 0.1$

Z_t ($Z_t = \zeta_t + i\xi_t$) in the target plane be related to its corresponding point Z ($Z = \zeta + i\xi$) in the initial plane via the function $f(Z_t)$. That is

$$Z = f(Z_t) \quad . \quad (6)$$

Our objective is to find the point Z , in the initial plane, that corresponds to a given target point, $Z_{t,0}$. We do this by constructing the function $f(Z_t)$. Since $f(Z_t)$ is an analytic function, it follows that a Taylor's series expansion of $f(Z_t)$ about the target point, $Z_{t,0}$, exists⁽⁵⁾, viz.

$$\begin{aligned} f(Z_t) = f(Z_{t,0}) &+ \frac{df(Z_{t,0})}{dZ_t} (Z_t - Z_{t,0}) \\ &+ \frac{d^2f(Z_{t,0})}{dZ_t^2} \frac{(Z_t - Z_{t,0})^2}{2!} + \dots + \frac{d^mf(Z_{t,0})}{dZ_t^m} \frac{(Z_t - Z_{t,0})^m}{m!} + \dots \end{aligned} \quad (7)$$

We begin by neglecting all terms in Eq. (7) higher than first order. Then we have

$$Z = B + C(Z_t - Z_{t,0}) \quad , \quad (8)$$

where B and C are complex constants and $Z_{t,0}$ is the given point in the target plane. We make two estimates of Z : Z_1 and Z_2 , and two estimates of the corresponding values of Z_t : $Z_{t,1}$ and $Z_{t,2}$. This yields four simultaneous equations:

5. G. F. Carrier, M. Krook, C. E. Pearson, Functions of a Complex Variable (McGraw-Hill Book Company, 1966). Sect. 2.6.

$$Z_1 = B + C (Z_{t,1} - Z_{t,0})$$

$$Z_2 = B + C (Z_{t,2} - Z_{t,0}) \quad (9)$$

which are solved for B. Our next estimate of Z is taken to be

$$Z_3 = B \quad (10)$$

By use of Z_3 , a trajectory is calculated and $Z_{t,3}$ is found. Equations (9) are solved for $B(=Z_4)$, etc. The procedure is continued until

$$|Z_{t,j} - Z_{t,0}| \leq \epsilon r_w \quad (11)$$

Here ϵ is a prescribed fractional multiple of the target plane window radius, r_w .

This start-up procedure uses the results of only the last two trajectory calculations to determine the next set of initial coordinates. When $j=5$, a least squares calculation, which uses all of the preceding results, takes over and is used thereafter. Both iteration procedures are described in more detail in Appendix A.

PARTICLE TRAJECTORY CALCULATION

The equations of motion of a heavy particle in a fluid are based on the assumption that the bulk fluid flow is not perturbed by the particles. Therefore, the particles move under influence of the forces of hydrodynamic drag, gravity, buoyancy, and inertial reaction of fluid carried along. For particles small enough for application of Stokes drag law, the theory is quite adequately developed. For larger particles, the theory is deficient and we must resort to approximate methods⁽⁶⁾.

6. N. A. Fuchs, The Mechanics of Aerosols, Translated by R. E. Daisley and M. Fuchs, edited by C. N. Davies (MacMillan, New York, 1964). Chapter III.

Davies and Aylward⁽⁷⁾ computed trajectories of small particles in flow about a plate, and Davies and Peetz⁽⁸⁾ performed similar calculations for flow around cylinders. More recently accurate calculations for small particle flow about spheres⁽⁹⁾ and plates⁽¹⁰⁾ have been reported.

Calculations for spherical particles of arbitrary size have been reported by: Langmuir and Blodgett for flow about spheres, cylinders, and ribbons⁽¹¹⁾; Dorsch et al. for flow about ellipsoids of revolution⁽¹²⁾; Norment for flow in nuclear clouds⁽¹³⁾; Etkin for air jets⁽¹⁴⁾; Morsi and Alexander for flow about cylinders and airfoils⁽¹⁵⁾; and Chai for airfoils⁽¹⁶⁾. All of these calculations are two-dimensional.

7. C. N. Davies and M. Aylward, "The Trajectories of Heavy, Solid Particles in a Two-Dimensional Jet of Ideal Fluid Impinging Normally upon a Plate," Proc. Phys. Soc. (London) B64, 889 (1951).
8. C. N. Davies and C. V. Peetz, "Impingement of Particles on a Transverse Cylinder," Proc. Roy. Soc. (London) A234, 269 (1956).
9. K. V. Beard and S. N. Grover, "Numerical Collision Efficiencies for Small Raindrops Colliding with Micron Size Particles," J. Atmos. Sci. 31, 543 (1974).
10. R. L. Pitter and H. R. Pruppacher, "A Numerical Investigation of Collision Efficiencies of Simple Ice Plates Colliding with Supercooled Water Drops," J. Atmos. Sci. 31, 551 (1974).
11. I. Langmuir and K. B. Blodgett, "Mathematical Investigation of Water Droplet Trajectories," General Electric Company, Report RL-225 (1945).
12. R. G. Dorsch, R. J. Brun, and J. L. Gregg, "Impingement of Water Droplets on an Ellipsoid with Fineness Ratio 5 in Axisymmetric Flow," NACA TN-3099 (March 1954). (Also see NACA TN-2952, 2999, 3047, 3155, 3410, 3153, 3586).
13. H. G. Norment, "Research on Circulation in Nuclear Clouds, II," Technical Operations, Inc., Report T0-B 64-102 (November 1964). AD-361 074.
14. B. Etkin, "Interaction of Precipitation with Complex Flows," Proceedings of the Third International Conference on Wind Effects on Buildings and Structures (Tokyo, 1971).
15. S. A. Morsi and A. J. Alexander, "An Investigation of Particle Trajectories in Two-Phase Flow Systems," J. Fluid Mech. 55, 193 (1972).
16. S. Kuo-Kai Chai, "Droplet Trajectories Around Aircraft Wing," Thesis, U. Nevada, Reno (November 1973).

If the particle density is large compared to the fluid, which is true for hydrometeors in air, we can neglect buoyancy and inertial reaction of the fluid to obtain the general equation

$$m \frac{d\vec{V}_p}{dt} = \frac{1}{2} \rho A_p (\vec{V}_f - \vec{V}_p) |\vec{V}_f - \vec{V}_p| C_D + m\vec{g} \quad (12)$$

where m is the particle mass, A_p the particle area projected in the direction of motion, \vec{V}_p particle velocity, \vec{V}_f fluid velocity, C_D drag coefficient, ρ fluid density, and \vec{g} gravity acceleration. Consider a flow of constant free-stream airspeed V around a body of characteristic dimension L .^{*} Then Eq. (12) can be non-dimensionalized to yield

$$\begin{aligned} \frac{dv_{px}}{d\tau} &= (v_{fx} - v_{px}) \frac{P}{P_T V_T F_N} \\ \frac{dv_{py}}{d\tau} &= (v_{fy} - v_{py}) \frac{P}{P_T V_T F_N} \\ \frac{dv_{pz}}{d\tau} &= (v_{fz} - v_{pz}) \frac{P}{P_T V_T F_N} - \frac{1}{F_N} \end{aligned} \quad (13)$$

Here length is scaled by L , velocity by V , and time by L/V , and

$$P = (C_D R_N^2) / R_N \quad (14)$$

$$F_N = V^2 / (Lg) \quad (15)$$

* Equivalent results are obtained by assuming either a moving body in a stationary fluid, or a moving fluid about a stationary body. Therefore we use whichever concept is most expedient.

$$R_N = \frac{\rho \delta}{\eta} \left| \vec{v}_p - \vec{v}_f \right| V \quad (16)$$

Non-dimensional quantities are:

\vec{v}_p, \vec{v}_f	particle and air velocities
τ	time
F_N	Froude number
R_N	Reynolds number
$C_D R_N^2 = B_N$	Best number
v_T	terminal settling speed (P_T is computed from v_T)

Dimensioned quantities are:

δ	particle dimension (sphere diameter or column base width)
ρ	air density
η	air viscosity
g	gravity acceleration constant
V	free-stream airspeed
L	characteristic dimension of body

In this form, the equations are applicable to any flow and to any size and shape of particle.*

* In the prior work cited above, most of the authors use some modification of these equations. For example, even though their trajectories are essentially horizontal in direction, Dorsch et al.⁽¹²⁾, Morsi and Alexander⁽¹⁵⁾, and Chai⁽¹⁶⁾ all neglect gravity. Etkin⁽¹⁴⁾ uses a constant P . Morsi and Alexander⁽¹⁵⁾ compute and use P independently for each space component, which is an incorrect procedure.

For Stokes drag ($R_N \leq 0.1$) P has the constant value 24. For larger R_N , P is a function of Reynolds number and acceleration; however the dependence on acceleration is not known. It is customary practice to use steady-state values of P , which are determined from terminal settling experiments. Use of these data are discussed in the chapter on Accuracy, and specifics regarding the data are presented in Appendix B.

Equations (13) are integrated numerically starting at a point far enough upstream that essentially free-stream conditions prevail. Krogh's ordinary differential equation integrator DVDQ⁽¹⁷⁾ is used. This code is recommended by Hull et al.⁽¹⁸⁾ and gives excellent results for this problem. The technique used to compute \vec{v}_f at each time step is described below.

THREE-DIMENSIONAL FLOW CALCULATION

In performing concentration factor calculations for sampling sites on particular airplanes it is important to use three-dimensional airflow. This is the only way to adequately account for particle settling, airplane geometry, angle-of-attack, airspeed and altitude.

Cloud physics airplanes are subsonic, sampling runs being made, typically between 100-150 kts. indicated airspeed. Particle measurement points are beyond the skin-friction boundary layer (see p.68), and should be placed to avoid separated flow regions. Therefore, potential (i.e., frictionless, incompressible, laminar) flow calculations are quite

-
17. F. T. Krogh, "Variable Order Integrators for Numerical Solution of Ordinary Differential Equations," Jet Propulsion Lab Technology Utilization Document No. CP-2308 (November 1970).
 18. T. E. Hull, W. H. Enright, B. M. Fellen, and A. E. Sedgwick, "Comparing Numerical Methods for Ordinary Differential Equations," SIAM J. Numer. Anal. 9, 603 (1972).

adequate. We use a code developed by Hess and Smith^(19,20) for calculating potential flow about arbitrary three-dimensional bodies. (Recent, more generalized methods reduce to the Hess-Smith procedure for comparable application⁽²¹⁾.) The Hess-Smith code requires input of a digital description of the aircraft surface. This consists of the coordinates of the corner points of a large number of contiguous, plane, quadrilaterals. An example of the digital description of a fuselage section is shown in Fig. 9.

The Hess-Smith code takes each quadrilateral panel to be a uniform-distributed source. On the basis of the boundary condition that there be zero flux through the centroid of each panel, and given the direction of the free-stream flow, the code finds the source strengths of all panels by inversion of a large matrix that includes all possible panel interactions. The matrix is inverted only once for each airplane geometry, provided that the results are stored for future use.

The concentration factor calculations require flow velocities, point-by-point along each trajectory. In calculating each flow velocity, contributions from all panels are summed. There are three algorithms for computing contributions: (1) for panels that are close to the calculation point, a detailed calculation is used that accounts for exact panel shape, (2) for panels at intermediate distances a multiple expansion is used, and (3) for remote panels a point source approximation is used.

-
19. J. L. Hess and A. M. O. Smith, "Calculation of Non-Lifting Potential Flow about Arbitrary Three-Dimensional Bodies," McDonnell Douglas Report E. S. 40622 (15 March 1962). AD-282 255.
 20. J. L. Hess and A. M. O. Smith, "Calculation of Potential Flow About Arbitrary Bodies," in Progress in Aeronautical Sciences, Vol. 8, edited by D. Kuchemann (Pergamon Press, New York, 1967).
 21. F. A. Woodward, "Analysis and Design of Wing-Body Combinations at Subsonic and Supersonic Speeds," J. Aircraft 5, 528 (1968).

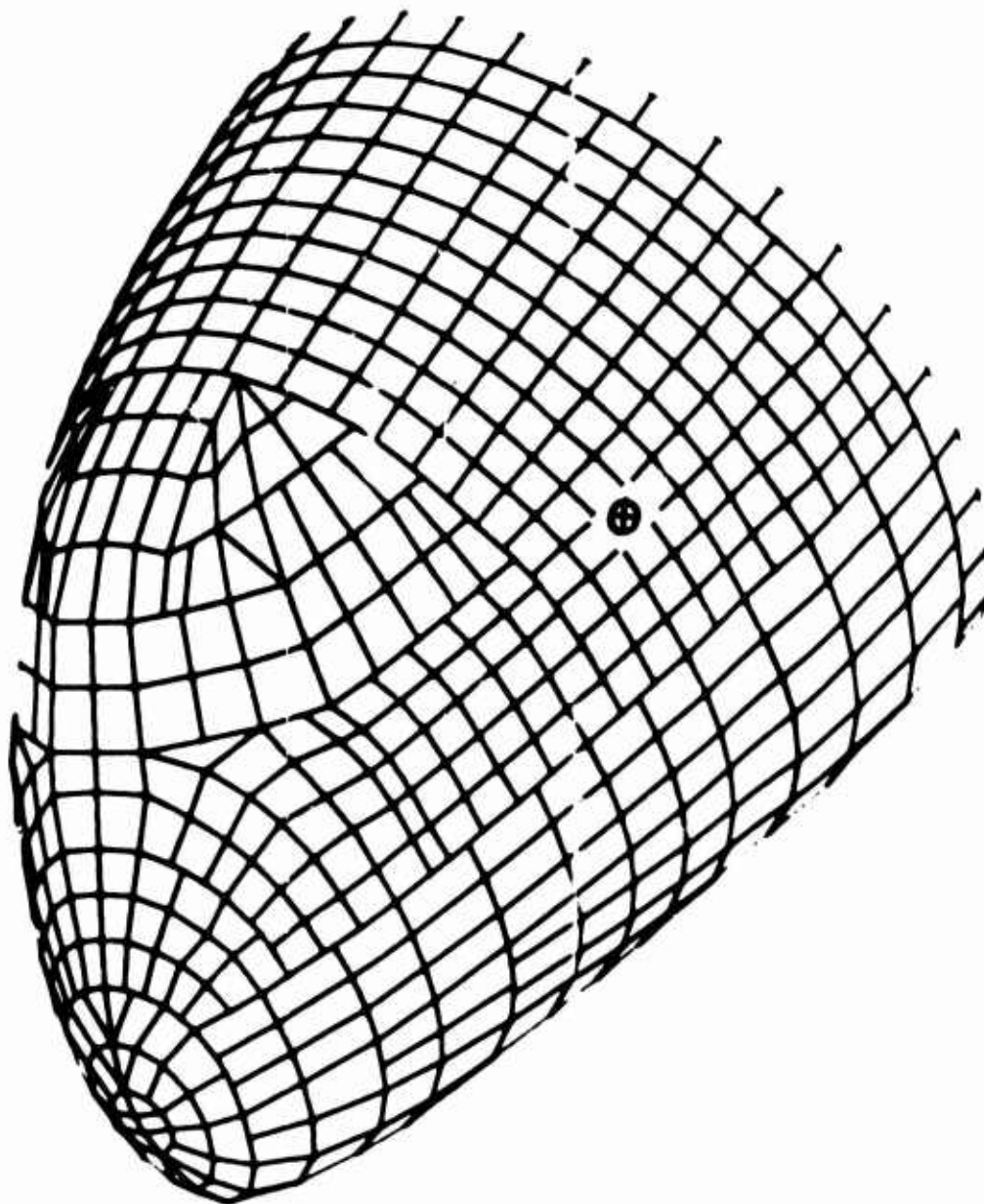


FIGURE 9. Computer-prepared plot of the digital description of the nose and cabin sections of the Lockheed C130A airplane. \otimes marks the location of the particle replicator.

To perform these calculations, we have developed a subroutine that consists of various extracted and modified portions of the Hess-Smith code. This subroutine is generalized such that given the source strength results for any three-dimensional body, it will provide \vec{v}_f for any input point (x,y,z). It also checks each input point to determine if it is inside the airplane body.

Hess and Smith have assessed the accuracy of their calculations for a number of body shapes and conditions; excellent agreement with both theory and experiment is found^(19,20). Our assessment is presented in the chapter on Accuracy. Of course accuracy depends on the fineness of resolution of the panel description of the body. Here some compromise is called for. The smaller the panels the finer the resolution, and the fewer of them for which the most exacting of the three algorithms must be used. On the other hand, the number of panels increases inversely as the square of their linear size. We have used the following criteria in setting up panel structures: For those parts of the airplane traversed by particle trajectories, we try to keep the panel edges between 6" to 8" in length (sampling, i.e. target, points are 9" to 15" from the fuselage). Where allowed by simplicity of surface shape, remote panels can be larger. Remote, downstream complexities, such as the wings and the tail, are ignored. The cylindrical portion of the fuselage is extended to approximately five times the length of the nose section, as recommended by Hess and Smith⁽²⁰⁾.

Computer time required for concentration factor calculation is largely dependent on the number of \vec{v}_f calculations required. On the CDC 6600 computer, one \vec{v}_f calculation requires on the order of 0.15 sec. The number of \vec{v}_f required per trajectory varies from about 60 to 300. A typical number of trajectories required is 25. Thus, computing time, even on a large computer, can be considerable.

HYDROMETEOR TYPES

WATER DROPS

From both theoretical and experimental viewpoints, by far the simplest hydrometeor to deal with is the water drop. Accordingly, confidence in concentration factor results for water drops is highest. For this reason our preliminary studies were done for water drops, and our "benchmark" results for all airplanes are for water drops.

Terminal settling speeds in air have been determined experimentally by Gunn and Kinzer⁽²²⁾, and confirmed by Beard and Pruppacher⁽²³⁾. Water drops smaller than about 400 μm in diameter are essentially spherical^(24,25). Since concentration factors for water drops larger than 400 μm are close to unity, we use drag data for spheres in our trajectory calculations. In this way we avoid having to cope with drop deformation effects at high altitudes, for which little data exists.

ICE CRYSTALS

From the ABRES Program viewpoint, interest in ice hydrometeors is probably greatest. Within limits imposed by local cloud conditions,

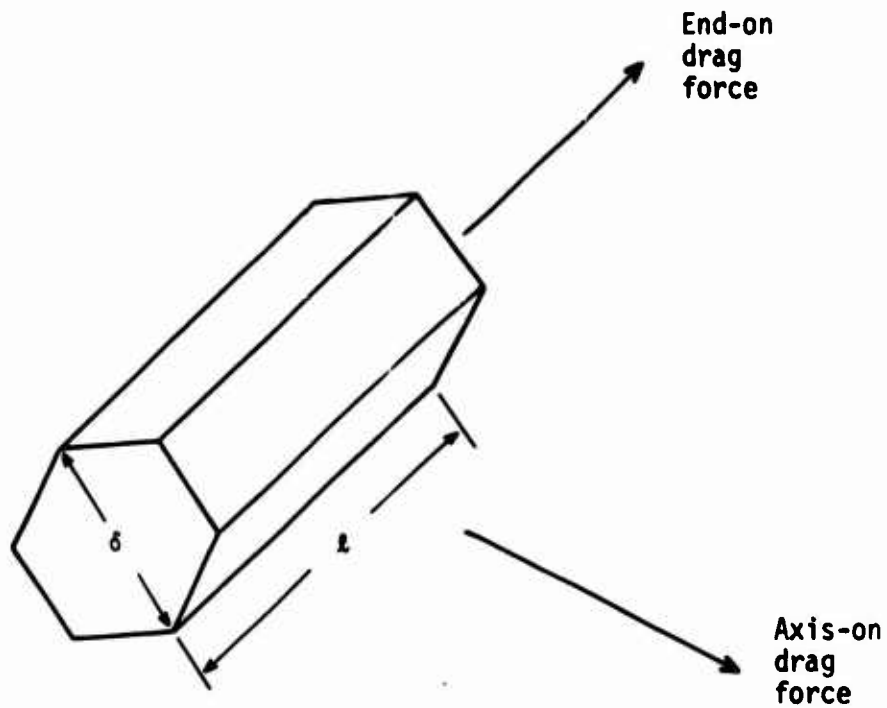
-
22. R. Gunn and G. D. Kinzer, "The Terminal Velocity of Fall for Water Droplets in Stagnant Air," J. Meteor. 6, 243 (1949).
 23. K. V. Beard and H. R. Pruppacher, "A Determination of the Terminal Velocity and Drag of Small Water Drops by Means of a Wind Tunnel," J. Atmos. Sci. 26, 1066 (1969).
 24. H. R. Pruppacher and K. V. Beard, "A Wind Tunnel Investigation of the Internal Circulation and Shape of Water Drops Falling at Terminal Velocity in Air," Quart. J. Roy. Met. Soc. 96, 247 (1970).
 25. H. R. Pruppacher and R. L. Pitter, "A Semi-Empirical Determination of the Shape of Cloud and Rain Drops," J. Atmos. Sci. 28, 86 (1971).

ice hydrometeors can assume any of a vast variety of geometrical forms⁽²⁶⁾. Nevertheless, certain systematics and trends have been established, and these can be used to reduce this problem to manageable portions. For example, under natural conditions water freezes to form crystals with hexagonal symmetry. Crystallization habits tend toward hexagonal based columns or plates. Moreover, whether plates or columns are produced seems to depend mostly on temperature⁽²⁶⁻²⁹⁾. More complex ice hydrometeor forms are either variations of these simple forms, more complex combinations of them, or very complex and essentially infinitely variable, dendritic forms.

To date, our work has concentrated on columns. There is considerable interest in this crystal form, especially since they are found to be the major constituent of cirrus clouds⁽³⁰⁾.

A number of studies of the dimensions of columnar ice have been reported. The most complete is that of Auer and Veal⁽³¹⁾, and we have chosen to use their results. Their equations relating the length, l , and base width, δ , (see Fig. 10) of natural ice columns are (dimensions in μm):

-
26. C. Magono and C. W. Lee, J. Fac. of Sci., Hokkaido U., Ser. VII, Vol. II, 321 (1966).
 27. N. H. Fletcher, The Physics of Rainclouds, (Cambridge University Press, 1966).
 28. B. J. Mason, The Physics of Clouds (Clarendon Press, Oxford, 1971).
 29. A. Ono, "Growth Mode of Ice Crystals in Natural Clouds," J. Atmos. Sci. 27, 649 (1970).
 30. A. J. Heymsfield and R. G. Knollenberg, "Properties of Cirrus Generating Cells," J. Atmos. Sci. 29, 1358 (1972).
 31. A. H. Auer and D. L. Veal, "The Dimension of Ice Crystals in Natural Clouds," J. Atmos. Sci. 27, 919 (1970).



Volume:

$$Vol = \frac{3\sqrt{3}}{8} \delta^2 l = 0.649519 \delta^2 l$$

Mass:

$$m = 0.649519 \delta^2 l \rho_p$$

Diameter of Water Drop of Equal Mass:

$$\delta_w = 1.0744786 (\delta^2 l \rho_p / \rho_{\text{water}})^{1/3}$$

FIGURE 10. Properties of hexagonal-based plates and columns

$$\delta = - 8.479 + 1.002\ell - 0.00234\ell^2 ; \quad \ell \leq 200 \mu\text{m}$$

$$\delta = 11.3\ell^{0.414} ; \quad \ell > 200 \mu\text{m} \quad (17)$$

Densities for solid and hollow ice columns were measured by Jayaweera and Ryan⁽³²⁾. They computed volumes from the dimensions of the individual crystals, and masses were estimated from the melted water drop diameters. The resulting densities were 0.7 g/cm^3 for solid columns, and 0.36 g/cm^3 for hollow columns. These densities are used in our calculations.

In free-fall settling experiments, columns are observed to orient their axes horizontally⁽³³⁾. Moreover, Bragg et al.⁽³⁴⁾ find for Reynolds numbers greater than about .05, that this orientation is assumed very rapidly. Accordingly, we take our column settling speed to be that for the horizontal orientation.

During trajectory calculations, we take the drag force vector to be parallel with $\vec{v}_f - \vec{v}_p$. Drag coefficient data exist for two column orientations relative to the drag force vector (see Appendix B). These orientations are shown in Fig. 10. In light of the overwhelming tendency of columns to fall with their axes horizontal, it is apparent that the "axis-on" orientation is the significant one. Nevertheless, we have computed concentration factors for both orientations.

It is important to realize that exceptions to the above are common. Substantial departures from stable horizontal settling are

32. K. O. L. F. Jayaweera and B. F. Ryan, "Terminal Velocities of Ice Crystals," *Quart. J. Roy. Met. Soc.* 98, 193 (1972).

33. K. O. L. F. Jayaweera and B. J. Mason, "The Behavior of Freely Falling Cylinders and Cones in a Viscous Fluid," *J. Fluid Mech.* 22, 709 (1965).

34. G. M. Bragg, L. van Zuider, and C. E. Hermance, "The Free-Fall of Cylinders at Intermediate Reynolds Numbers," *Atmos. Environ.* 8, 755 (1974).

reported by Jayaweera and Mason for asymmetrically loaded models⁽³⁵⁾, and by Zikmunda and Vali⁽³⁶⁾ for rimed ice columns observed in the field.

At any particular point in space, such as a measurement (target) point, it is not possible to predict with assurance the orientation of a column axis in the horizontal plane. Our best assumption is that this orientation is variable. A Knollenberg particle spectrometer will register a projection of the column dimension in the direction perpendicular to its linear sensing array. If we assume a random column orientation in the horizontal, then we show in Appendix C that the ensemble mean projected dimension of a column, $\langle v \rangle$, is

$$\langle v \rangle = \frac{2}{\pi} (\ell + \delta) \quad (18)$$

where ℓ and δ are as defined in Fig. 10. We feel that $\langle v \rangle$ provides reasonable approximations to mean values of column dimensions registered by a Knollenberg spectrometer.

Properties of the ice columns studied are given in Table 3. Work on ice plates is underway, but not far enough along to allow us to include results here. We also plan to treat other, more complicated shapes such as spatial dendrites.

35. K. O. L. F. Jayaweera and B. J. Mason, "The Falling Motions of Loaded Cylinders and Discs Simulating Snow Crystals," *Quart. J. Roy. Met. Soc.* 92, 151 (1966).

36. J. Zikmunda and G. Vali, "Fall Patterns and Fall Velocities of Rimed Ice Crystals," *J. Atmos. Sci.* 29, 1334 (1972).

TABLE 3
COLUMNAR CRYSTAL PROPERTIES

Length, l (μm)	Width, δ (μm)	δ/l	$\langle V \rangle$	Solid Columns*		Hollow Columns*	
				Mass (μg)	Diameter of water drop of equal mass (μm)	Mass (μg)	Diameter of water drop of equal mass (μm)
50	35.8	.715	54.62	.0291	38.1	.0149	30.6
70	50.2	.717	76.52	.0802	53.5	.0412	42.9
85	59.8	.703	92.18	.138	64.1	.0710	51.4
100	68.3	.683	107.14	.212	74.0	.1091	59.3
120	78.1	.650	126.11	.332	86.0	.171	68.9
140	85.9	.614	143.81	.470	96.5	.242	77.3
160	91.9	.575	160.36	.615	105.5	.316	84.5
200	93.4	.492	189.97	.880	118.9	.453	95.3
300	117.0	.390	265.47	1.87	152.8	.960	122.4
380	129.1	.340	324.10	2.88	176.5	1.480	141.4
500	144.5	.289	410.30	4.75	208.5	2.441	167.1
700	165.9	.237	551.25	8.76	255.8	4.505	204.9
900	183.6	.204	689.84	13.8	297.6	7.094	238.4
1000	197.3	.1973	762.2	17.7	323.3	9.100	259.0
1500	226.5	.151	1099.12	35.0	405.8	17.99	325.1
2000	262.8	.1314	1440.5	62.8	493.3	32.32	395.2
3000	310.9	.104	2107.8	131.9	631.5	67.82	506.0
4000	350.2	.088	2769.4	223.1	752.4	114.72	602.8

* Solid column density is taken to be 0.7 g/cm^3 , and hollow column density is taken to be 0.36 g/cm^3 .

RESULTS

PARTICLE REPLICATOR ON THE LOCKHEED C130A

The particle replicator arm⁽²⁾ exits the C130A fuselage in the cabin section just aft of the cockpit, at the location marked in Fig. 9 and as shown in Fig. 11. It is mounted perpendicular to the fuselage symmetry plane. As determined by measurement on the airplane, the particle intake slit is 14.3 inches from the fuselage, measured along the arm.

Our digital description of the C130A fuselage was developed from Lockheed engineering drawings of moldline contours. Accuracy of individual coordinates is several hundredths of an inch. Aft of the cabin section, the fuselage is formed from sections of two circular cylinders. The complete fuselage description is shown in Fig. 12. A total of 1264 quadrilateral panels are used in this description.

Engineering drawings of airplanes are based on a coordinate system that appears to be, in part, a relic of shipbuilding. The fuselage axis coordinate is called the fuselage station, FS; perpendicular to the FS axis we have: in the horizontal the bunline axis, BL, and in the vertical the waterlevel axis, WL. The C130A nose tip is at FS=61", the bulkhead that separates the cabin from the cylindrical part of the fuselage is at FS=245", the fuselage symmetry plane is at BL=0, and the cabin flight deck, as well as the center of the principal circular cylinder (of radius 85") is at WL=200". In this system the replicator slit has coordinates:

$$FS = 176.87"$$

$$BL = 85.45"$$

$$WL = 225.74"$$

In the airflow and trajectory computations, we take the origin at:

$$FS = 245"$$

$$BL = 0$$

$$WL = 200"$$



FIGURE 11. Lockheed C130A with formvar replicator arm
in position (flowplate not mounted)

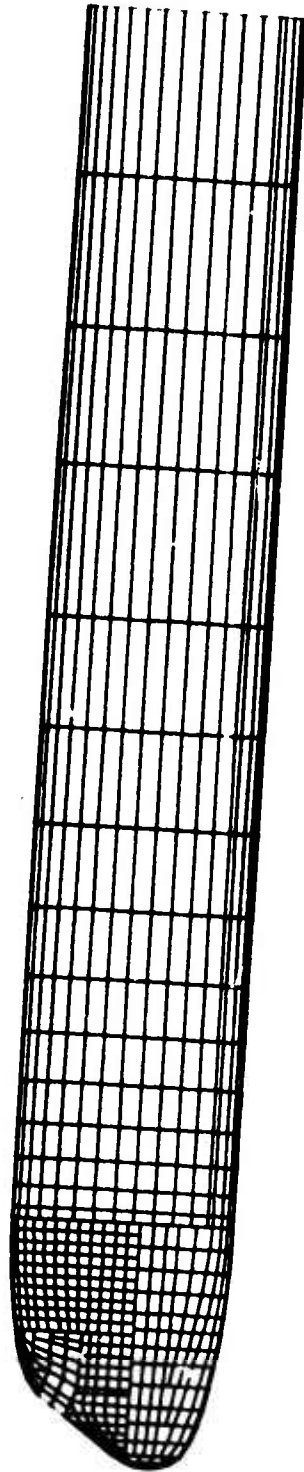


FIGURE 12. Computer-prepared plot of the digital description of the complete Lockheed C130A fuselage. The upward tilt of the nose represents a 4° angle-of-attack.

The characteristic dimension of the airplane, L (see discussion of Eqs. (13)), is taken as the length of the cabin section, $L=184"$. This is the distance from the tip of the nose to the cabin bulkhead. All linear measures are normalized by this length.

Concentration factors for water drops at and near the replicator slit at 5 kft, and at the slit at 30 kft, are shown in Fig. 13 and listed in Table 4. Flight conditions are given in Table 1. According to these results the replicator is mounted in a relatively favorable place, in the sense that drops of all sizes are sampled; but certainly it is not free of concentration distortion. This distortion is clearly evident in the stereographic plots shown in Fig. 14. In these plots an enlarged particle flux tube is shown as it reaches the replicator slit. Contraction of the tube relative to its upstream shape is apparent (also see Fig. 8). Measured fluxes are about 40% higher than their free-stream values for drops between 60-100 μm diameter, depending on altitude. This represents concentration distortion of about 30% as obtained by dividing C_F by v_T (Table 2). Moreover, only very small and very large drops are free of the effect. The shift of concentration factor peak to smaller particle sizes as altitude is increased is a typical trend.

Concentration factors for solid and hollow ice columns at the replicator slit at 5 kft altitude are plotted in Figs. 15-18 and listed in Tables 5 and 6. Properties of the ice crystals are given in Table 3. Calculations were done for both the "axis-on" and "end-on" orientations with respect to the drag vector (Fig. 10). Terminal settling with long axis horizontal was used for both orientations. As is evident in Figs. 15-18, there are large differences in results for the two orientations, the end-on concentration factors for the large columns being considerably smaller. As noted above (p. 27), the axis-on orientation is observed to be the stable one in free-fall settling experiments. Moreover, Bragg et al.⁽³⁴⁾ observe that this orientation is assumed very rapidly for columns large enough to be of interest here. Therefore, we consider only the axis-on results to be significant, and ignore the end-on results hereafter.

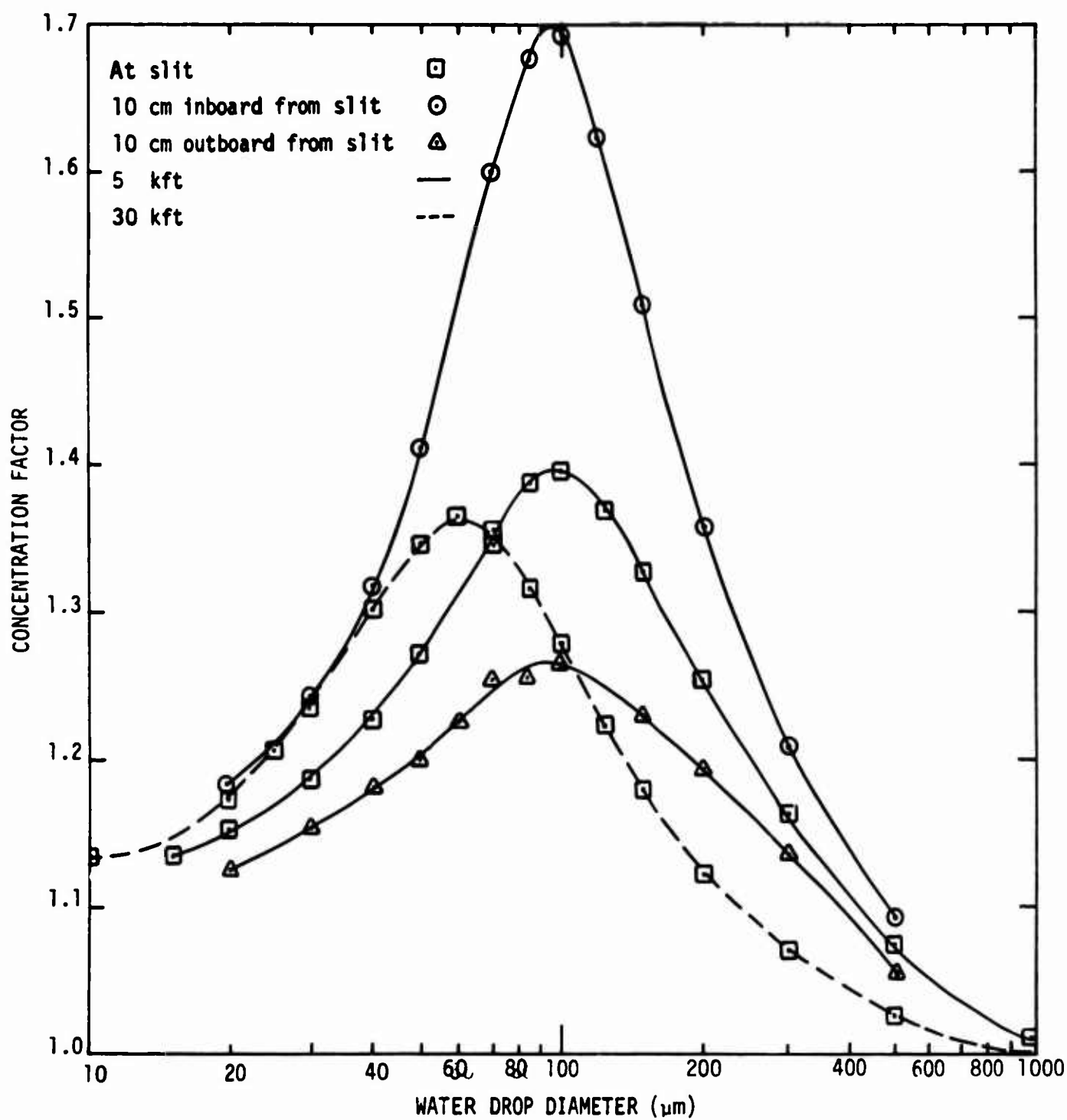


FIGURE 13. Water drop concentration factors at and near the particle replicator slit on the Lockheed C130A

TABLE 4

WATER DROP CONCENTRATION FACTORS AT AND NEAR THE
 REPLICATOR SLIT ON THE LOCKHEED C130A
 (See Table 1 for flight conditions)

Drop diameter (μm)	Concentration Factors			30 kft altitude
	5 kft altitude			
		10 cm inboard*	10 cm outboard*	
	<u>Slit</u>	<u>from slit</u>	<u>from slit</u>	<u>Slit</u>
10				1.132
15	1.136			
20	1.153	1.184	1.126	1.176
25				1.206
30	1.186	1.241	1.153	1.236
40	1.226	1.317	1.180	1.300
50	1.271	1.412	1.200	1.346
60			1.225	1.365
70	1.346	1.600	1.253	1.353
85	1.389	1.677	1.255	1.314
100	1.397	1.693	1.266	1.277
120		1.623		
125	1.370			1.223
150	1.327	1.509	1.230	1.179
200	1.252	1.358	1.192	1.121
300	1.162	1.208	1.135	1.070
500	1.072	1.093	1.058	1.024
1000	1.010			.998

* Distances from the replicator slit are along the replicator arm.

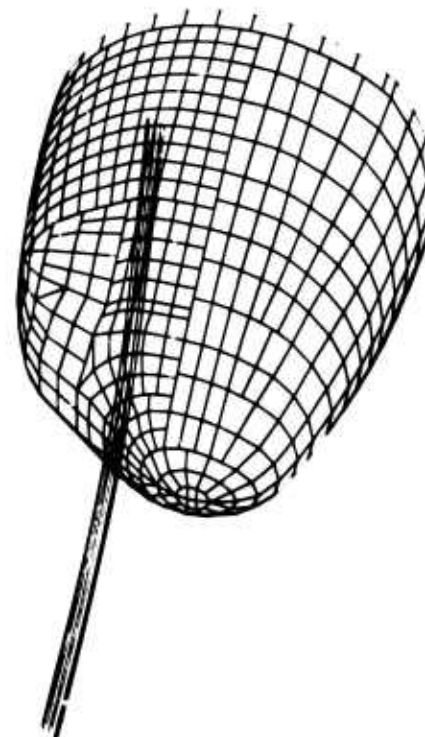
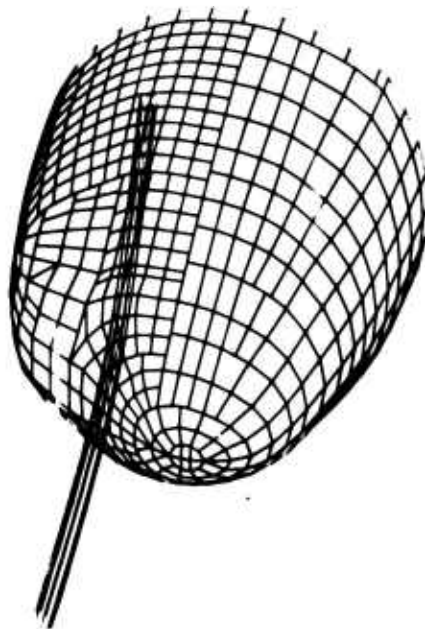


FIGURE 14a. Stereographic plots of an eight-trajectory, 20 μ m-diameter water drop flux tube to the Lockheed C130A particle replicator slit. The central trajectory is also shown. $C_F = 1.15$.

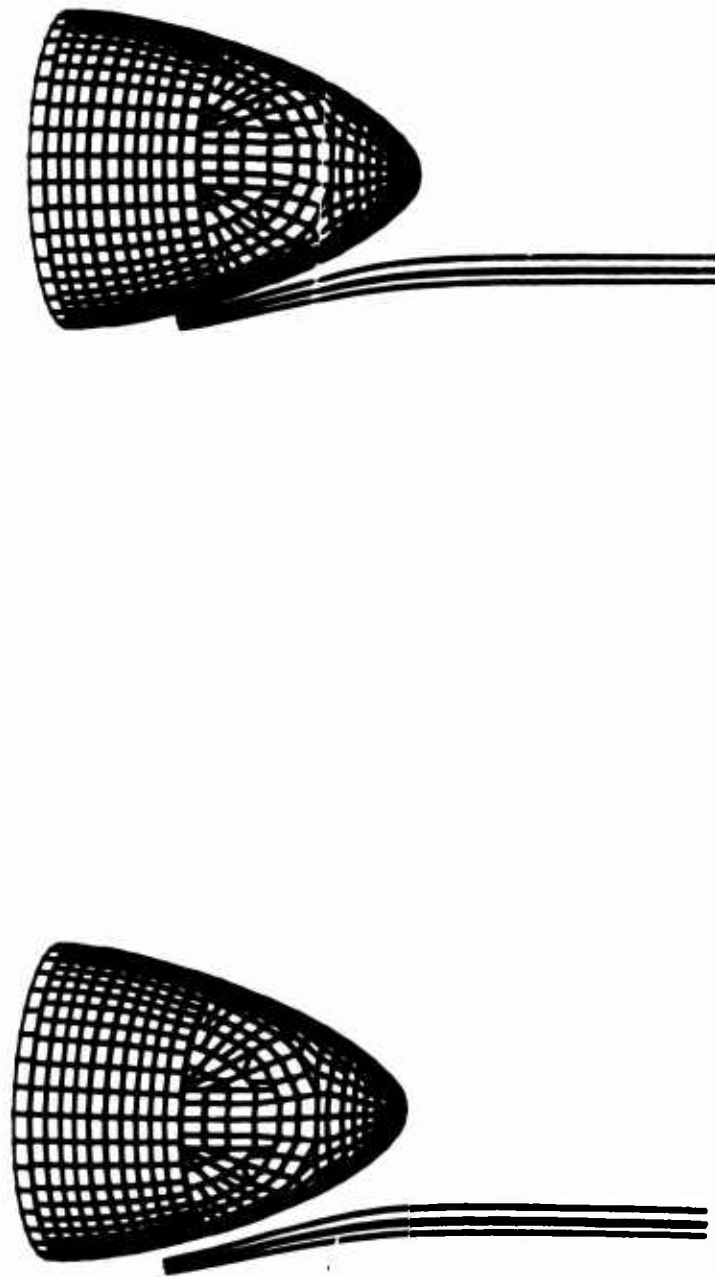


FIGURE 14b. Stereographic plots of a six-trajectory, 100 μm -diameter water drop flux tube to the Lockheed C130A particle replicator slit. The central trajectory also is shown.

$$r_w = .02, \quad \epsilon = .05, \quad C_F = 1.41.$$

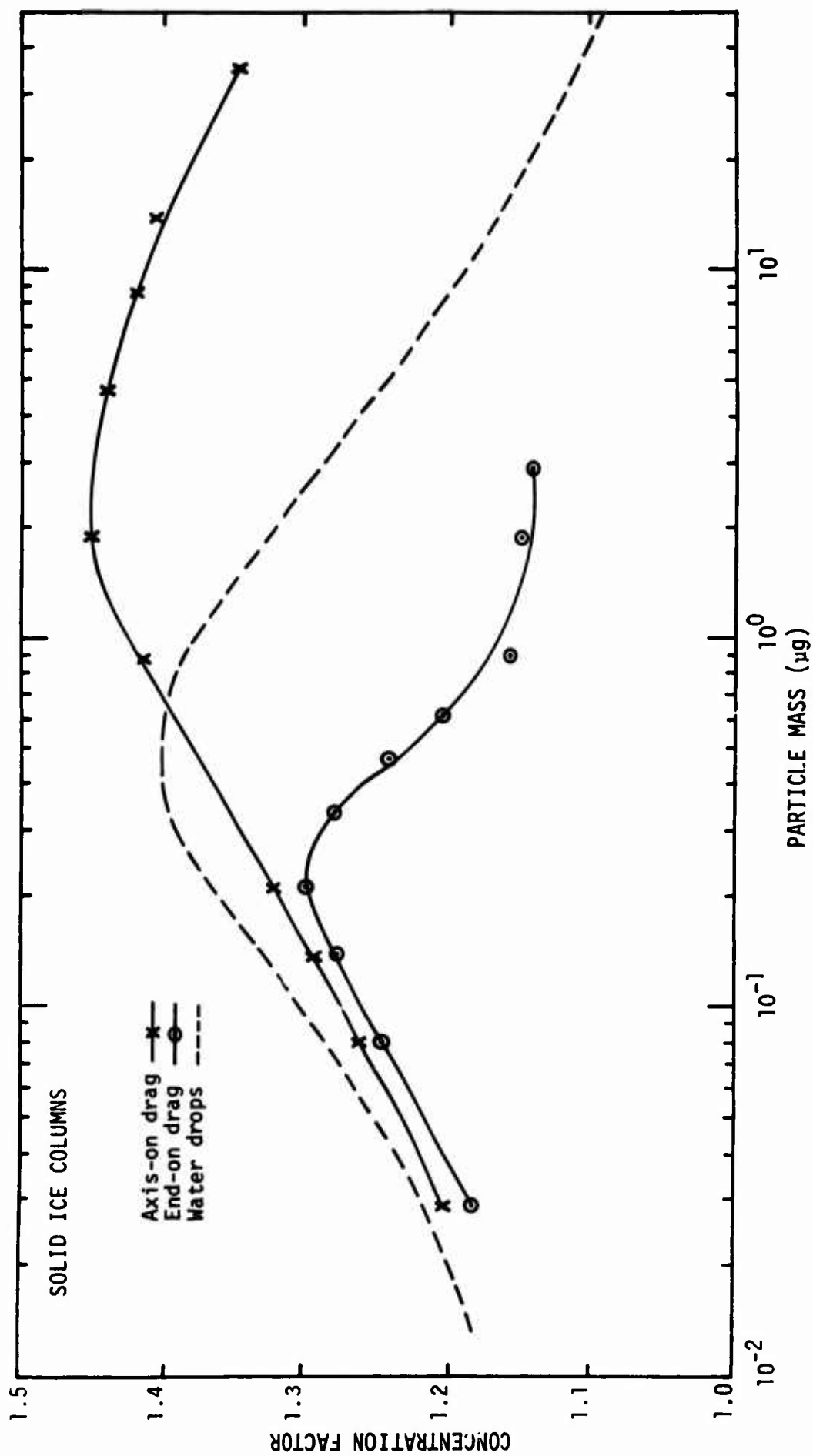


FIGURE 15.. Concentration factor vs. particle mass for solid ice columns ($\rho_p = 0.7 \text{ g/cm}^3$) at the particle replicator slit on the Lockheed C130A. Altitude is 5 kft.

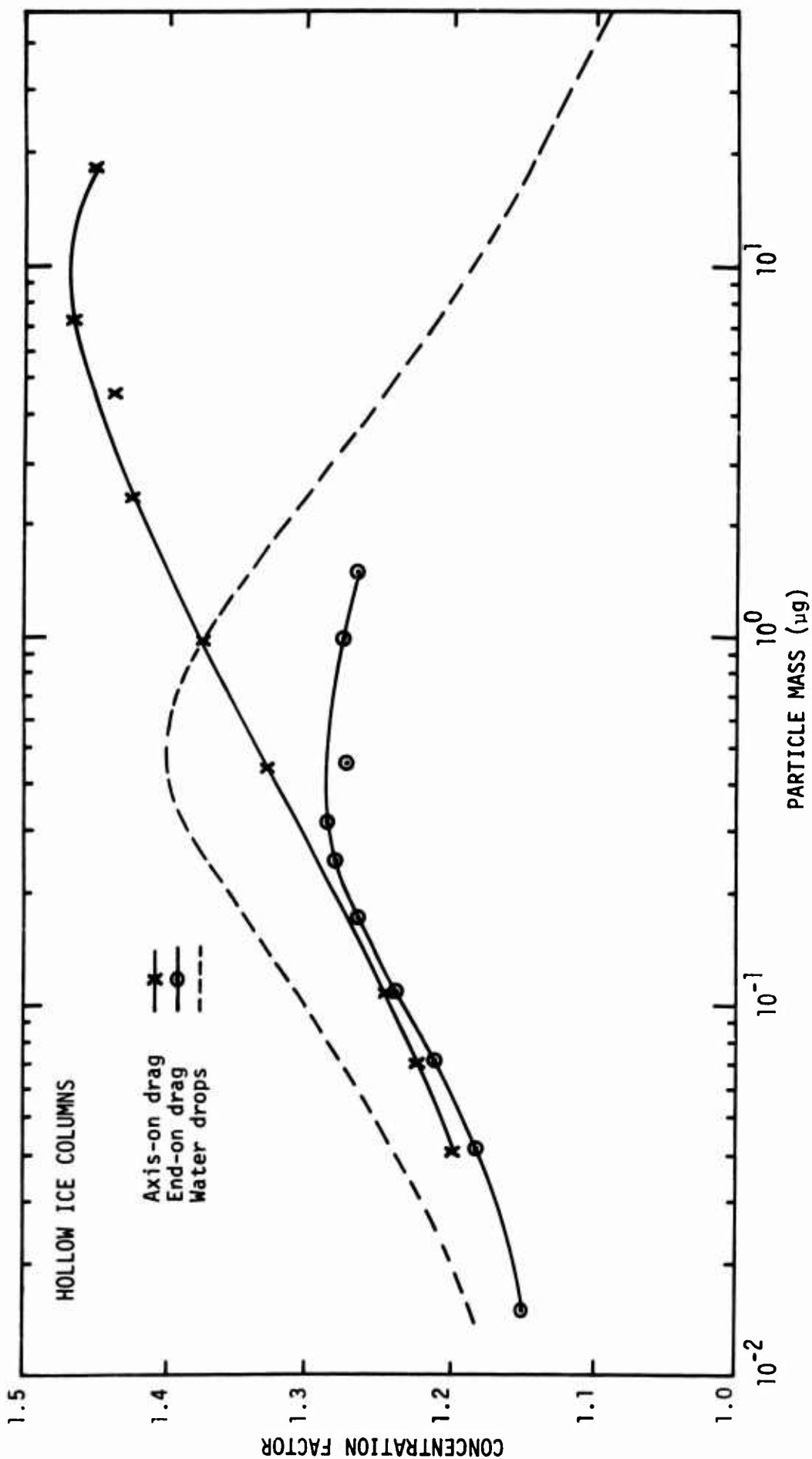


FIGURE 16. Concentration factor vs. particle mass for hollow ice columns ($\rho_p = 0.36 \text{ g/cm}^3$) at the particle replicator slit on the Lockheed C130A. Altitude is 5 kft.

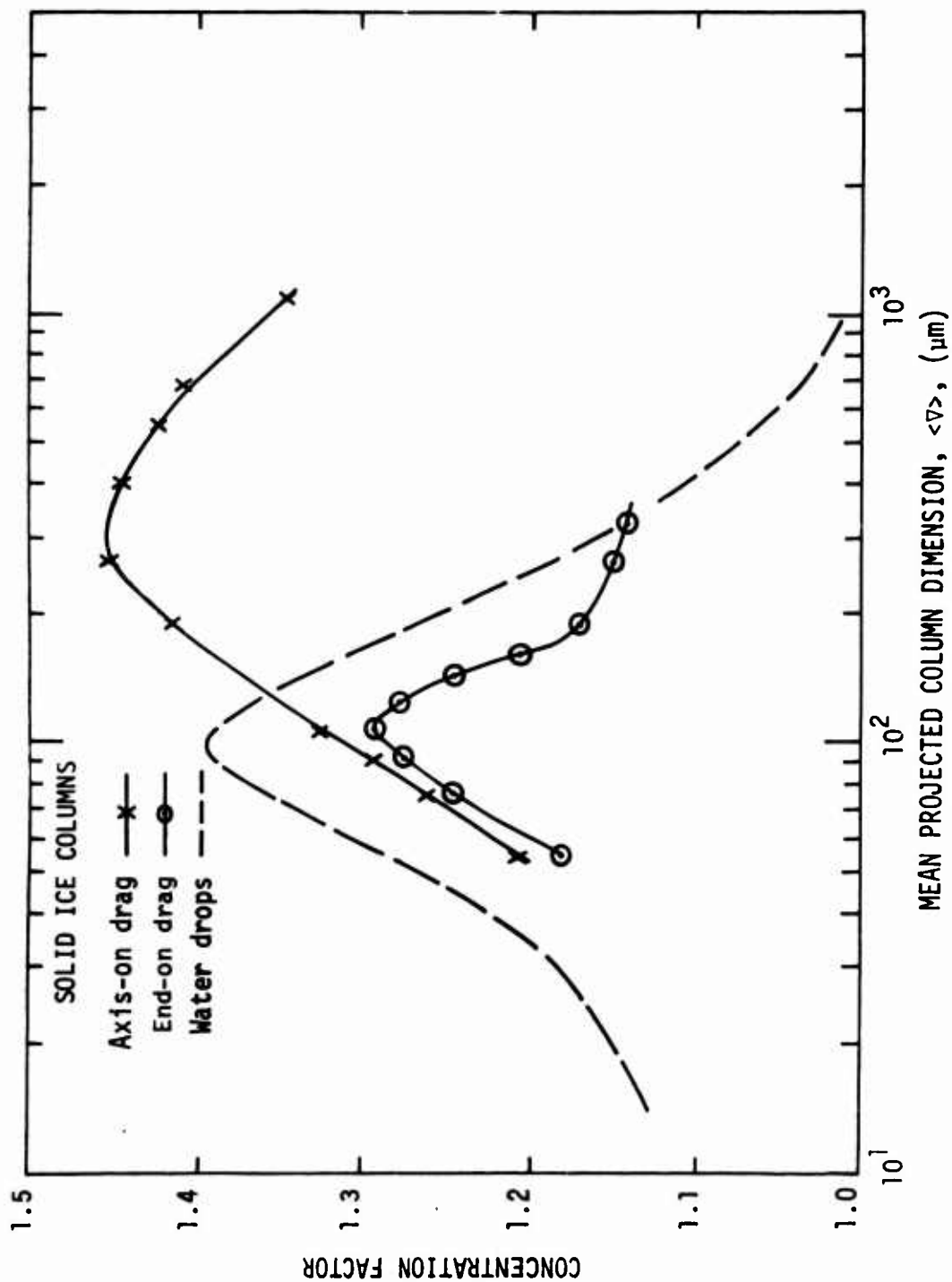


FIGURE 17. Concentration factor vs. mean projected column dimension for solid ice columns ($\rho_p = 0.7 \text{ g/cm}^3$) at the particle replicator slit on the Lockheed C130A. Altitude is 5 kft.

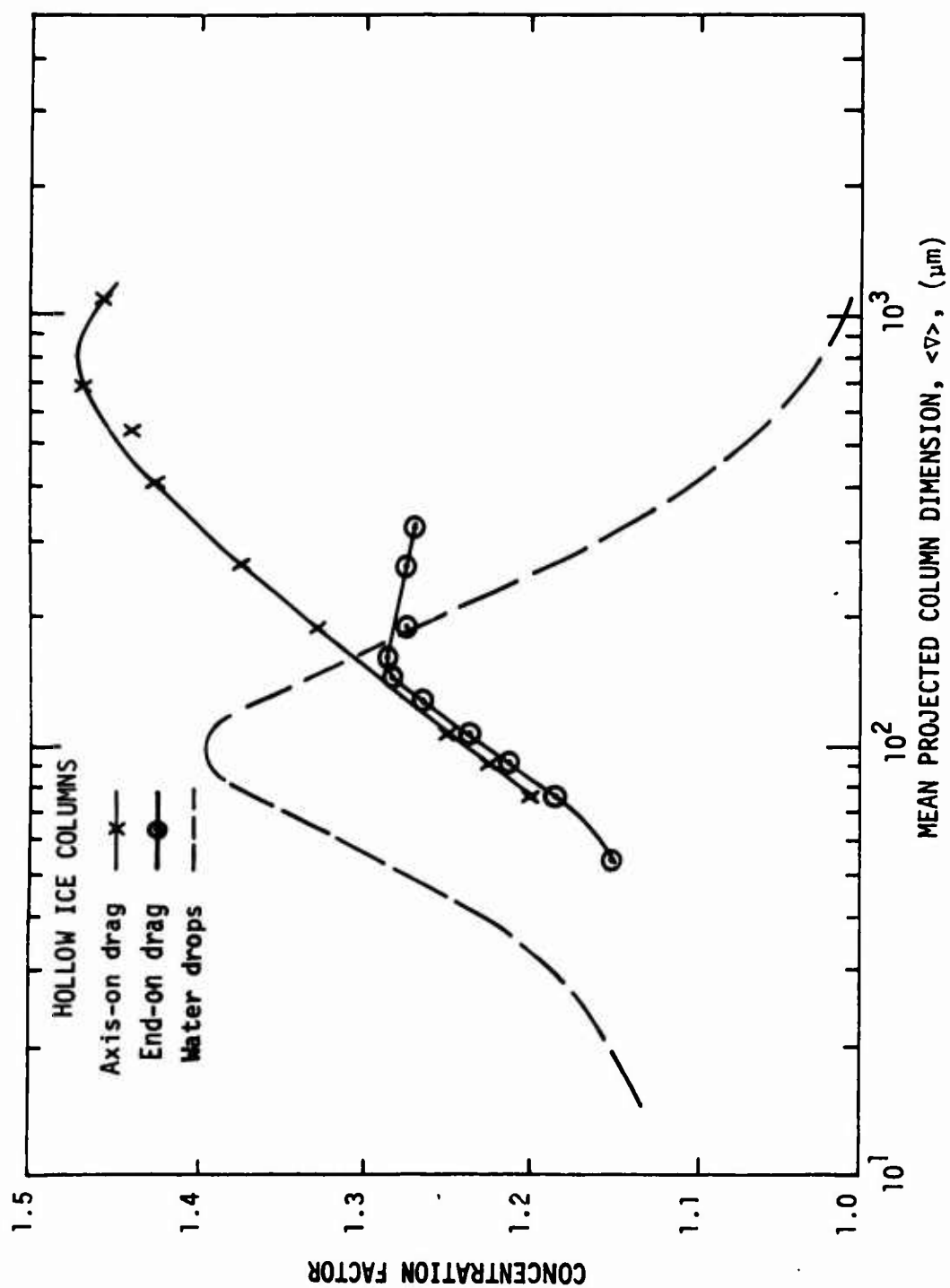


FIGURE 18. Concentration factor vs. mean projected column dimension for hollow ice columns ($\rho_p = 0.36 \text{ g/cm}^3$) at the particle replicator slit on the Lockheed C130A. Altitude is 5 kft.

TABLE 5

ICE COLUMN CONCENTRATION FACTORS AT THE PARTICLE REPLICATOR
SLIT ON THE LOCKHEED C130A (AXIS-ON DRAG)Altitude = 5 kft
(see Tables 1 and 3)

Length, ℓ (μm)	Width, δ (μm)	Concentration Factors	
		Solid Columns	Hollow Columns
50	35.8	1.207	
70	50.2	1.260	1.199
85	59.8	1.291	1.223
100	68.3	1.323	1.244
200	98.3	1.416	1.329
300	117.0	1.451	1.375
500	144.0	1.443	1.426
700	166.0	1.423	1.439
900	184.0	1.408	1.467
1500	227.0	1.348	1.453

TABLE 6

ICE COLUMN CONCENTRATION FACTORS AT THE PARTICLE REPLICATOR
SLIT ON THE LOCKHEED C130A (END-ON DRAG)Altitude = 5 kft
(see Tables 1 and 3)

Length, ℓ (μm)	Width, δ (μm)	Concentration Factors	
		Solid Column	Hollow Column
50	35.8	1.183	1.151
70	50.2	1.244	1.185
85	59.8	1.276	1.212
100	68.3	1.295	1.235
120	78.1	1.278	1.264
140	85.9	1.243	1.282
160	91.9	1.206	1.284
200	98.4	1.155	1.272
300	117.0	1.151	1.274
380	129.1	1.142	1.269

Water drop results also are plotted in Figs. 15-18 for comparison with those of the ice columns. We see that the ice curves peak at larger C_F values and for larger particles than for water drops. In terms of the mean projected column dimension (see p. 28), the curves peak at $\sim 300 \mu\text{m}$ for solid columns and $\sim 800 \mu\text{m}$ for hollow columns. Maximum concentration distortion of about 30% is indicated, with slightly smaller distortions distributed over a wide range of particle sizes.

PARTICLE REPLICATOR ON THE LOCKHEED C130E

On this airplane the replicator arm exits the fuselage through a window in the forward cargo compartment. The replicator arm is perpendicular to the fuselage axis, but not horizontal; its geometry is shown in Fig. 19. The coordinate system (FS, BL, WL) is identical to the one used for the C130A, and we use the same origin and scaling factor for our computations (see pp. 30, 33). The replicator location is shown in Fig. 20.

The C130A digital description was modified to allow for the C130E nose radome and the different trajectory paths. Quadralateral spacing is as discussed for the C130A. A total of 1692 quadralaterals are used in this description. The complete fuselage is shown in Fig. 21.

Concentration factor calculations were made for water drops at 5 kft altitude. Flight conditions are given in Table 1. Results are shown in Fig. 22 and listed in Table 7. Our calculations indicate that water drops over a diameter range of about $90\text{-}300 \mu\text{m}$ cannot be sampled at the replicator slit. The calculations crudely define the shadow zone indicated by the shaded region in Fig. 22. The replicator arm is being lengthened by 8" to alleviate this problem; however, even at this distance the calculations indicate substantial concentration distortion.

Stereographic trajectory plots are shown in Fig. 23. These trajectories are to a point 10 cm outboard from replicator slit, measured along the replicator arm. Deflection and flux distortion are evident, the concentration factor at this point being 2.5. The cause of the shadow zone is obvious. Trajectories closest to the airplane almost

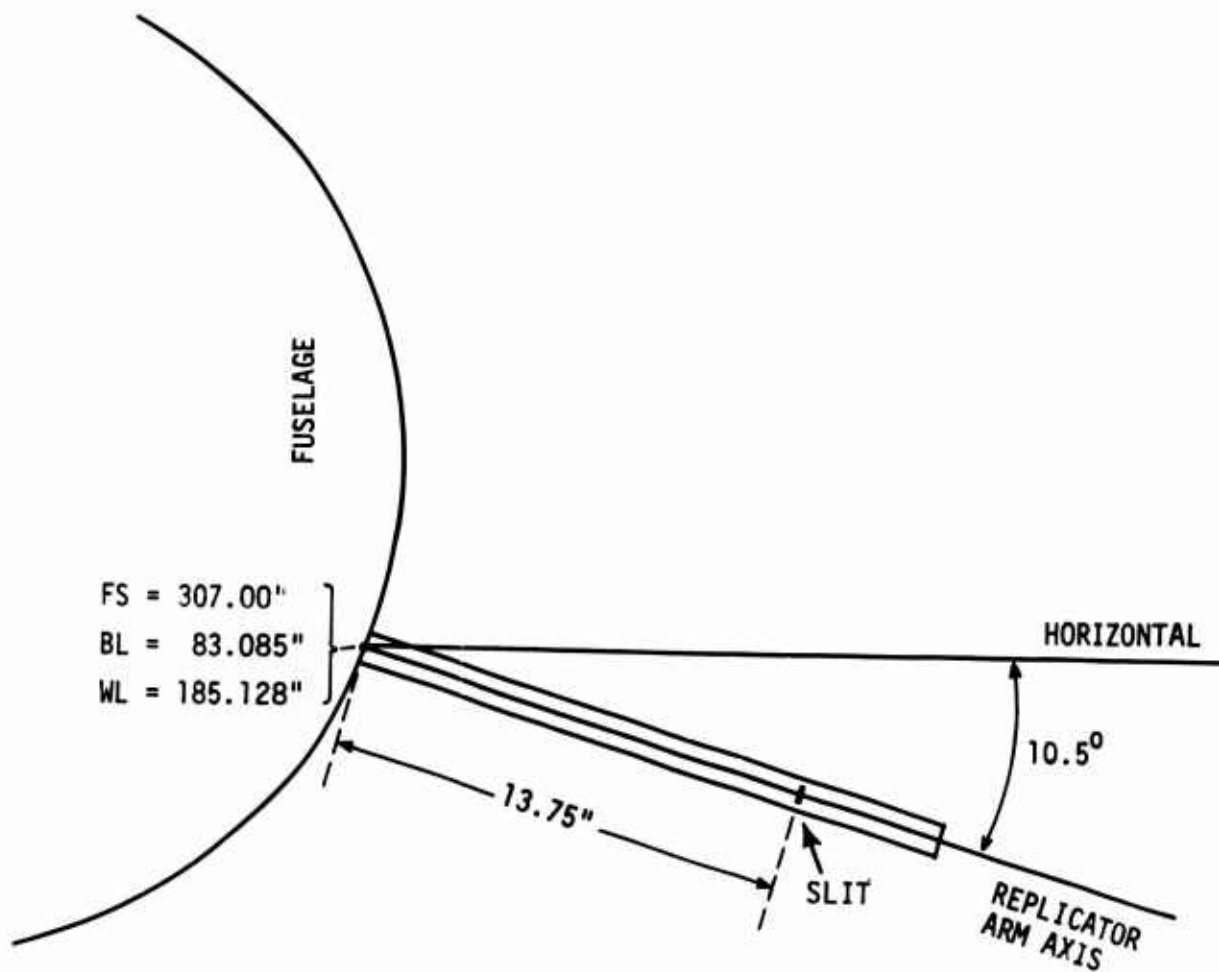


FIGURE 19. Particle replicator arm geometry on the Lockheed C130E.
(Not drawn to scale.)

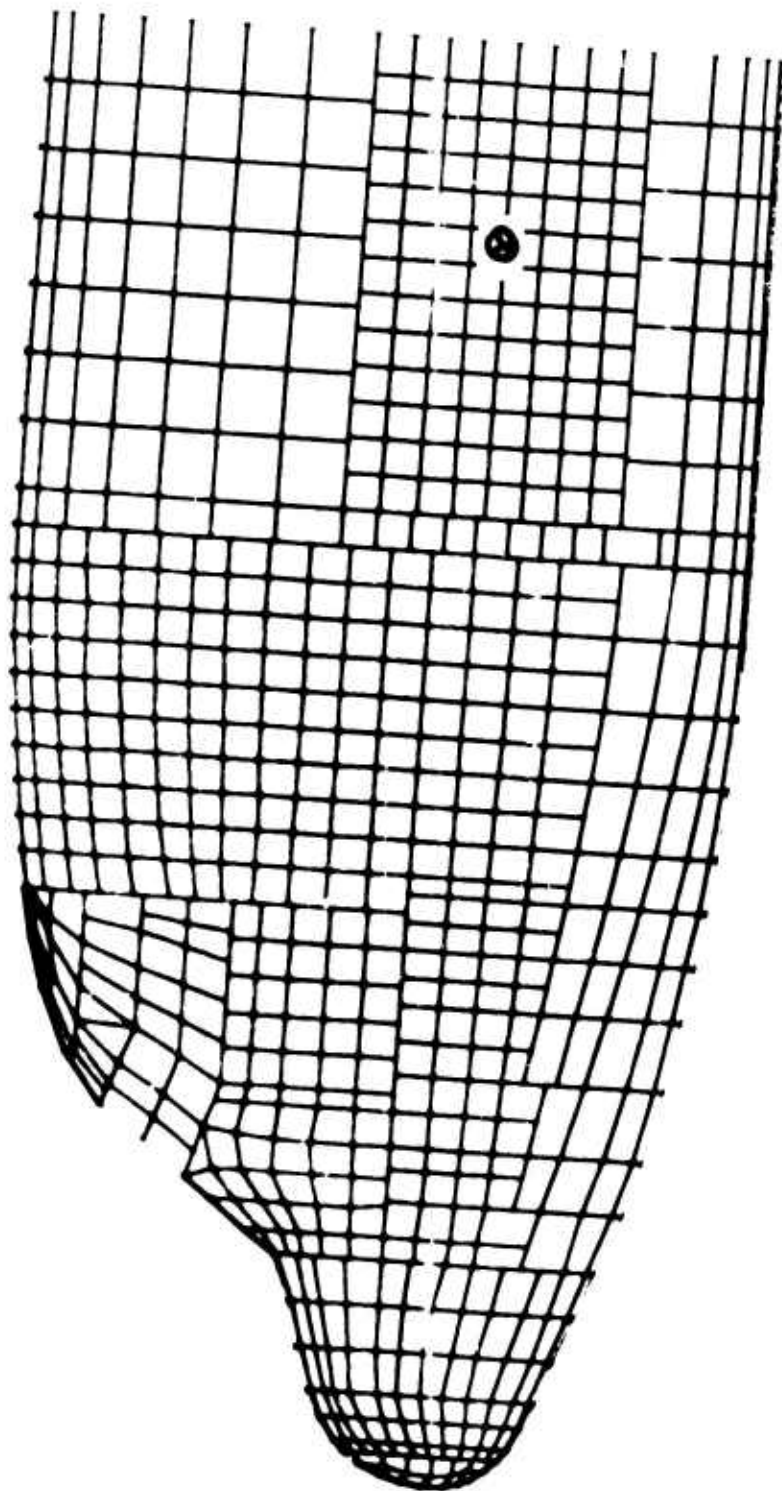


FIGURE 20. Computer-prepared plot of the digital description of the Lockheed C130E forward fuselage to FS 350". X marks the location of the particle replicator.

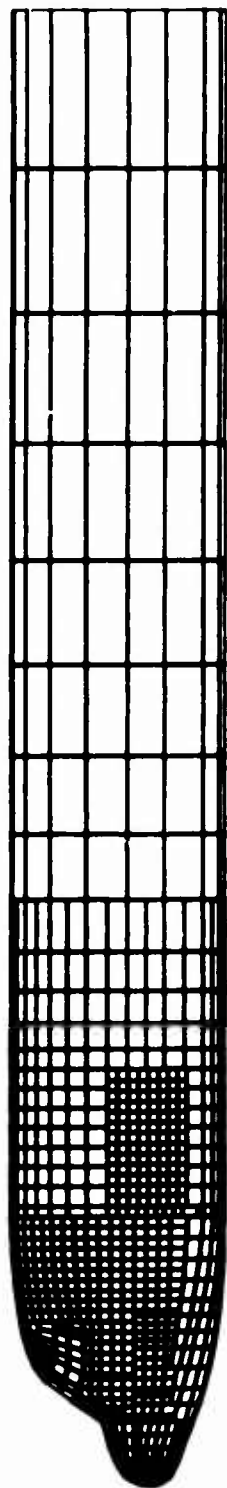


FIGURE 21. Computer-prepared plot of the digital description of the complete Lockheed C130E fuselage

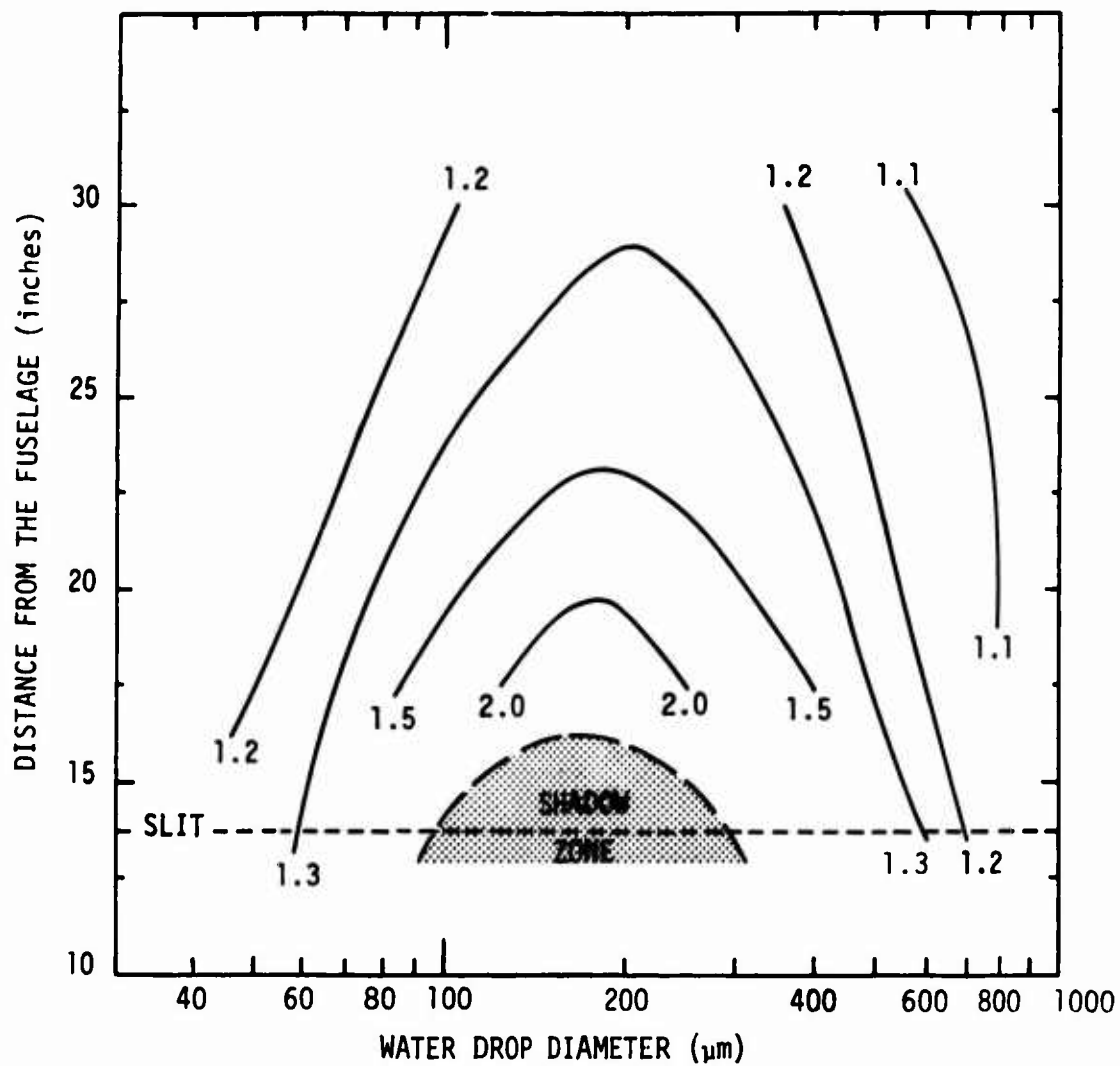


FIGURE 22. Concentration factor contours vs. water drop diameter along the particle replicator arm on the Lockheed C130E

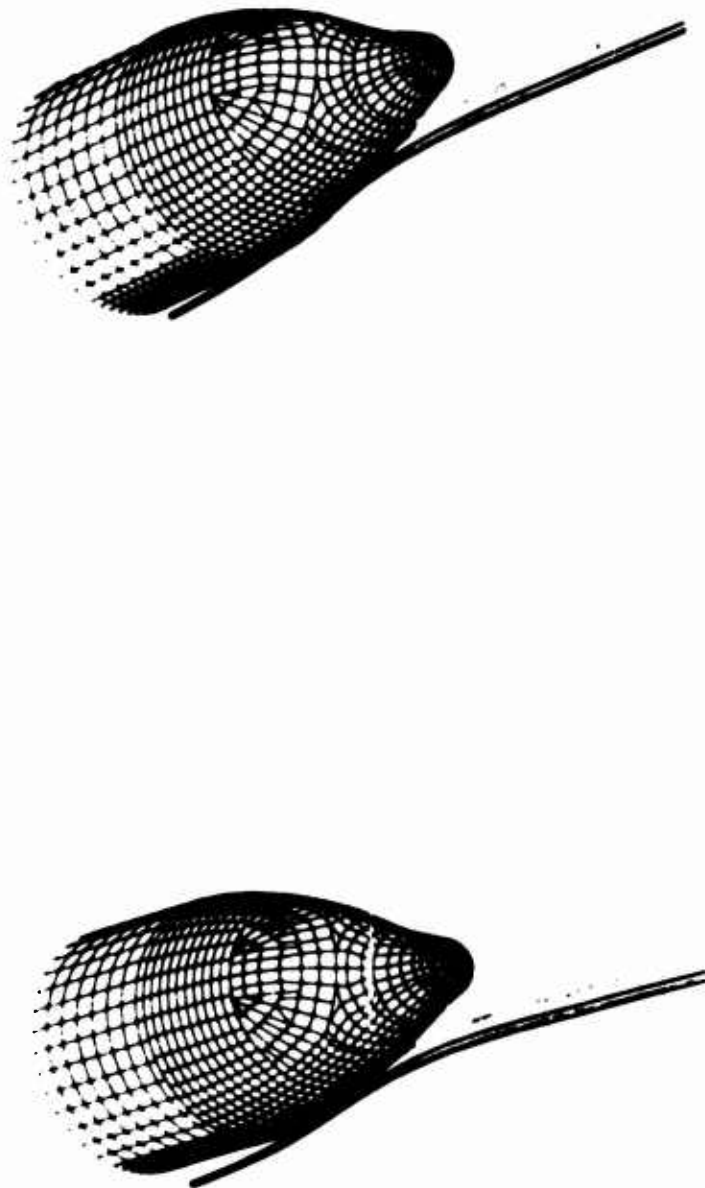


FIGURE 23a. Stereographic plots of a six-trajectory, 150 μm-diameter flux tube to a point 10 cm outboard from the Lockheed C130E particle replicator slit. The central trajectory also is shown.

$$r_w = .01, \epsilon = .2, C_F = 2.54$$

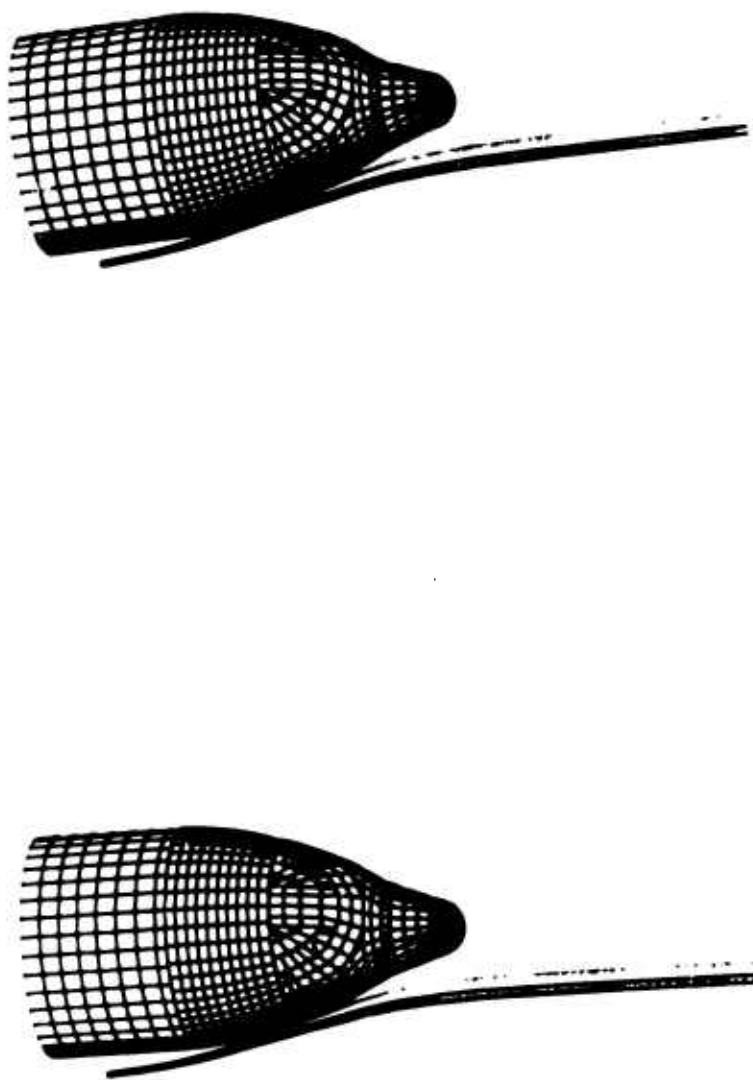


FIGURE 23b. Stereographic plots of a six-trajectory, 150 μ m-diameter flux tube to a point 10 cm outboard from the Lockheed C130E particle replicator slit. The central trajectory also is shown.

$$r_w = .01, \epsilon = .2, C_F = 2.54$$

TABLE 7

WATER DROP CONCENTRATION FACTORS FOR THE REPLICATOR
ON THE LOCKHEED C130E

(see Table 1 for flight conditions)

Water drop diameter (μm)	Distance from the Fuselage Along the Replicator Arm (inches)				
	Slit				
	<u>13.75</u>	<u>17.687</u>	<u>21.624</u>	<u>25.561</u>	<u>29.489</u>
50	1.265	1.187	1.148	1.123	1.106
70	~1.40	1.319	1.228	1.176	1.145
100	--	1.630	1.366	1.262	1.204
150	--	2.460	1.568	1.370	1.275
200	--	2.299	1.578	1.386	1.289
300	--	1.719	1.443	1.322	1.248
500	1.401	1.272	1.202	1.154	1.117
600	1.272				
700	1.201				
800	1.157	1.117	1.089	1.069	1.052

graze the fuselage. It is clear that drops of this size cannot reach the replicator since they are intercepted by the fuselage in an area below the cabin.

KNOLLENBERG PARTICLE SPECTROMETERS ON THE CESSNA CITATION

The Knollenberg particle spectrometers are mounted on the emergency exit door in the forward part of the passenger cabin (Figs. 24 and 25). The precipitation particle spectrometer has a particle size range 200-3000 μm , and the cloud particle spectrometer has a particle size range 20-300 μm . Measurement points are 9" from the fuselage for both instruments. Both instruments are mounted with their axes perpendicular to the fuselage symmetry plane.

The fuselage description (Figs. 25 and 26) was developed from dimensioned, line drawings taken from a brochure. The drawings were enlarged and copied to graph paper by use of a Kargel Reflecting Projector. Individual coordinate values are accurate to within $2\frac{1}{2}$ ", though rather extensive interpolation was required in some sections. On most of the fuselage, especially the parts traversed by particles, quadrilateral panel edges were kept to about 6". A total of 1304 panels are used in the complete fuselage description.

The nose and cockpit part of the fuselage is 10' long. The passenger cabin is a circular tube with a radius of 2.65'. The particle spectrometers are 14' aft of the nose tip.

Coordinate measurements were taken in a (FS, BL, WL) coordinate system with FS=0 at the nose tip, and the fuselage axis at BL=0, WL=4.25'. In this system the centers of the optical paths of the particle spectrometers are:

precipitation particle spectrometer —

FS = 13.95'

BL = 3.40'

WL = 4.25'



FIGURE 24. Cloud physics instrumentation mounted on the Cessna Citation. The uppermost and lowermost instruments are the cloud particle and precipitation particle spectrometers, respectively. (Photo courtesy of Meteorology Research, Inc.)

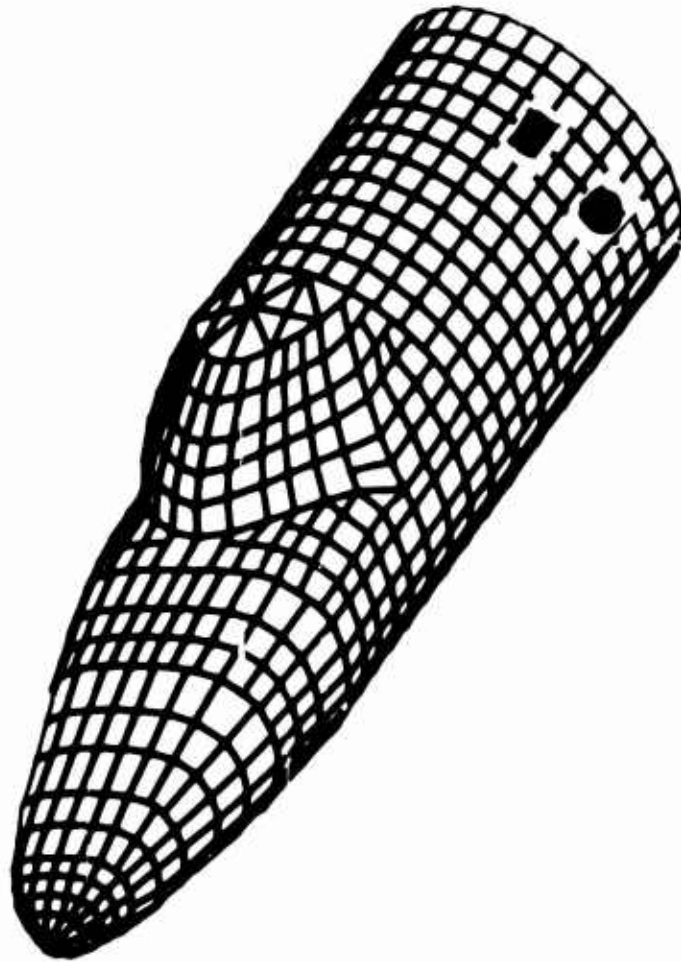


FIGURE 25. Computer-prepared plot of the digital description of the forward fuselage of the Cessna Citation. The precipitation particle spectrometer location is marked with ● and the cloud particle spectrometer with ■

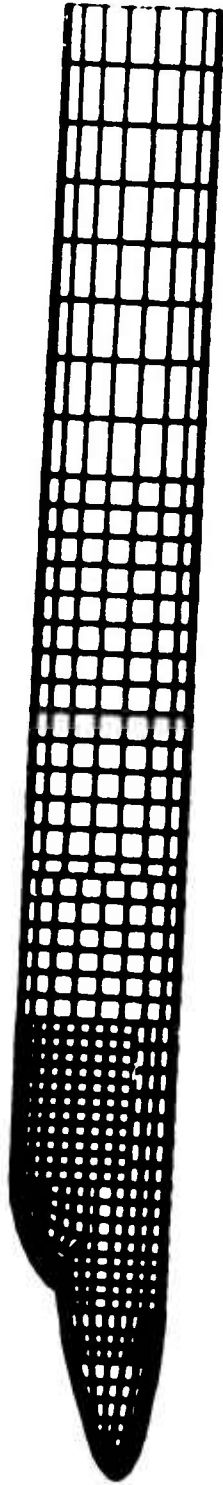


FIGURE 26. Computer-prepared plot of the complete Cessna Citation fuselage description.
The upward tilt of the nose represents a 3° angle-of-attack.

cloud particle spectrometer —

$$FS = 13.95'$$

$$BL = 3.056'$$

$$WL = 5.807'$$

For computer calculations, the origin of coordinates is:

$$FS = 10'$$

$$BL = 0$$

$$WL = 4.25'$$

The characteristic length of the airplane, L , by which all linear measures are normalized (see discussion of Eqs. (13)), is 10 feet.

Water drop concentration factors for the particle spectrometers are plotted in Fig. 27 and listed in Table 8. Flight conditions are given in Table 1. Extensive calculations also were done for ice columns. Results are plotted in Figs. 28-31 and are listed in Table 9.

Serious problems exist at both spectrometers, but particularly at the cloud particle spectrometers. From Fig. 32 we see that particles must undergo considerable trajectory deflection to reach the target points. At the precipitation particle spectrometer, concentration distortion ranges from 60-80%. For the cloud particle spectrometer, the deflection point is closer to the spectrometer and the deflection is more abrupt, which explains the more serious problem at this spectrometer. At the cloud particle spectrometer a narrow shadow zone between ~ 100 - $120 \mu\text{m}$ is indicated for water drops. For ice columns at the cloud particle spectrometer, there is a shadow zone above $\sim 300 \mu\text{m}$ mean projected dimension for solid columns, and $\sim 800 \mu\text{m}$ for hollow columns. Large concentration distortions are indicated for smaller columns.

The situation here is similar to that of the C130E replicator. The target points are far removed from the free stream: being too far aft and too close to the fuselage. Figure 32 suggests the possibility of a flow separation problem at the cloud particle spectrometer, though our method does not allow investigation of this possibility. It is clear that both spectrometers, particularly the cloud particle spectrometer, are very unfavorably mounted.

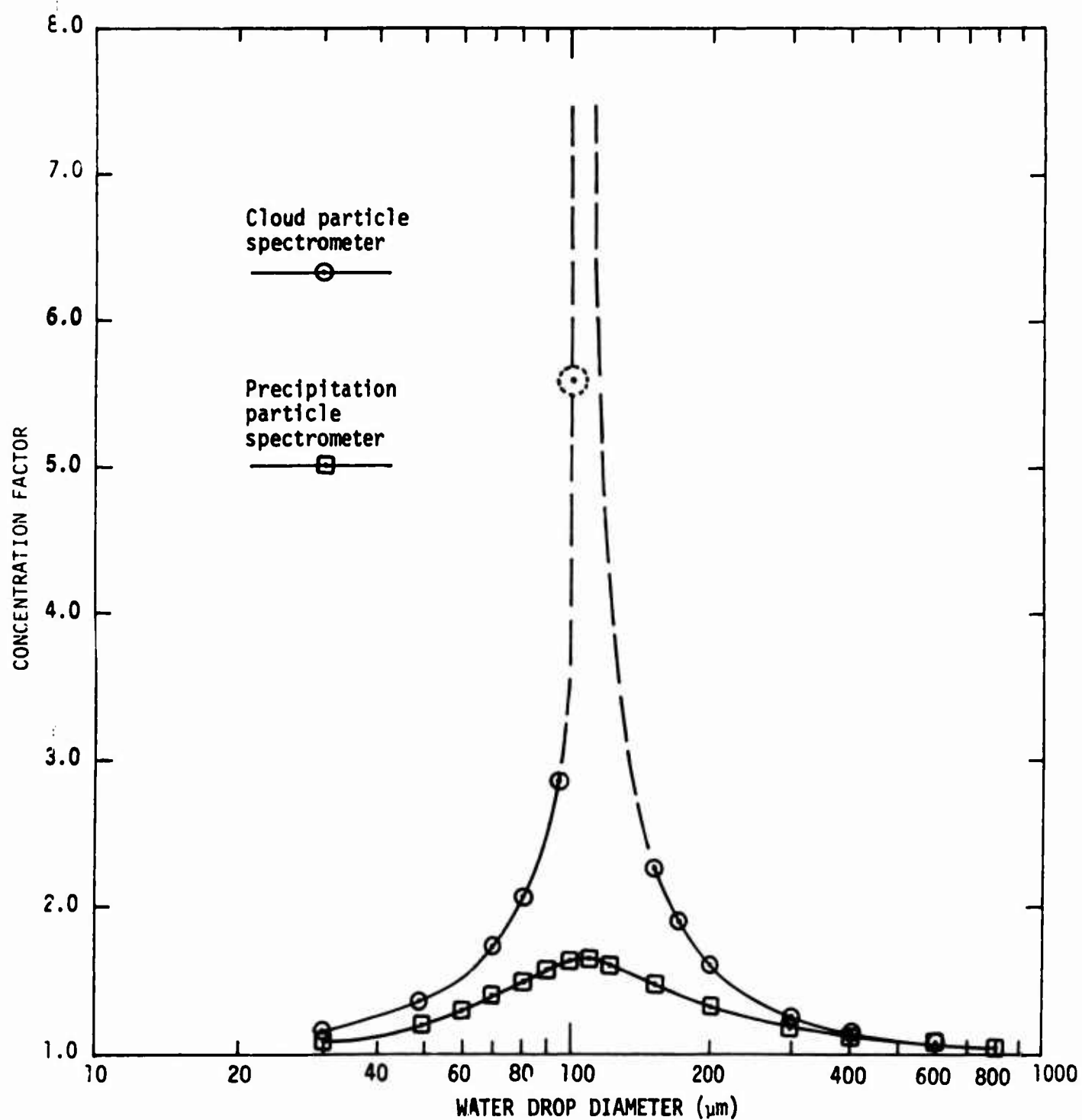


FIGURE 27. Concentration factors vs. water drop diameters for the Knollenberg particle spectrometers on the Cessna Citation. The point marked (○) is hand-calculated from a partial result.

TABLE 8

WATER DROP CONCENTRATION FACTORS FOR THE PARTICLE
SPECTROMETERS ON THE CESSNA CITATION

(see Table 1 for flight conditions)

<u>Water drop diameter</u>	<u>Precipitation Particle Spectrometer</u>	<u>Cloud Particle Spectrometer</u>
30	1.079	1.126
50	1.198	1.328
60	1.281	
70	1.380	1.712
80	1.480	2.076
90	1.564	
95		2.827
100	1.622	~5.6*
110	1.645	
120	1.614	
150	1.482	2.286
170		1.880
200	1.324	1.601
300	1.182	1.270
400	1.112	1.159
600	1.046	1.066
800	1.018	

* Estimated from partial results

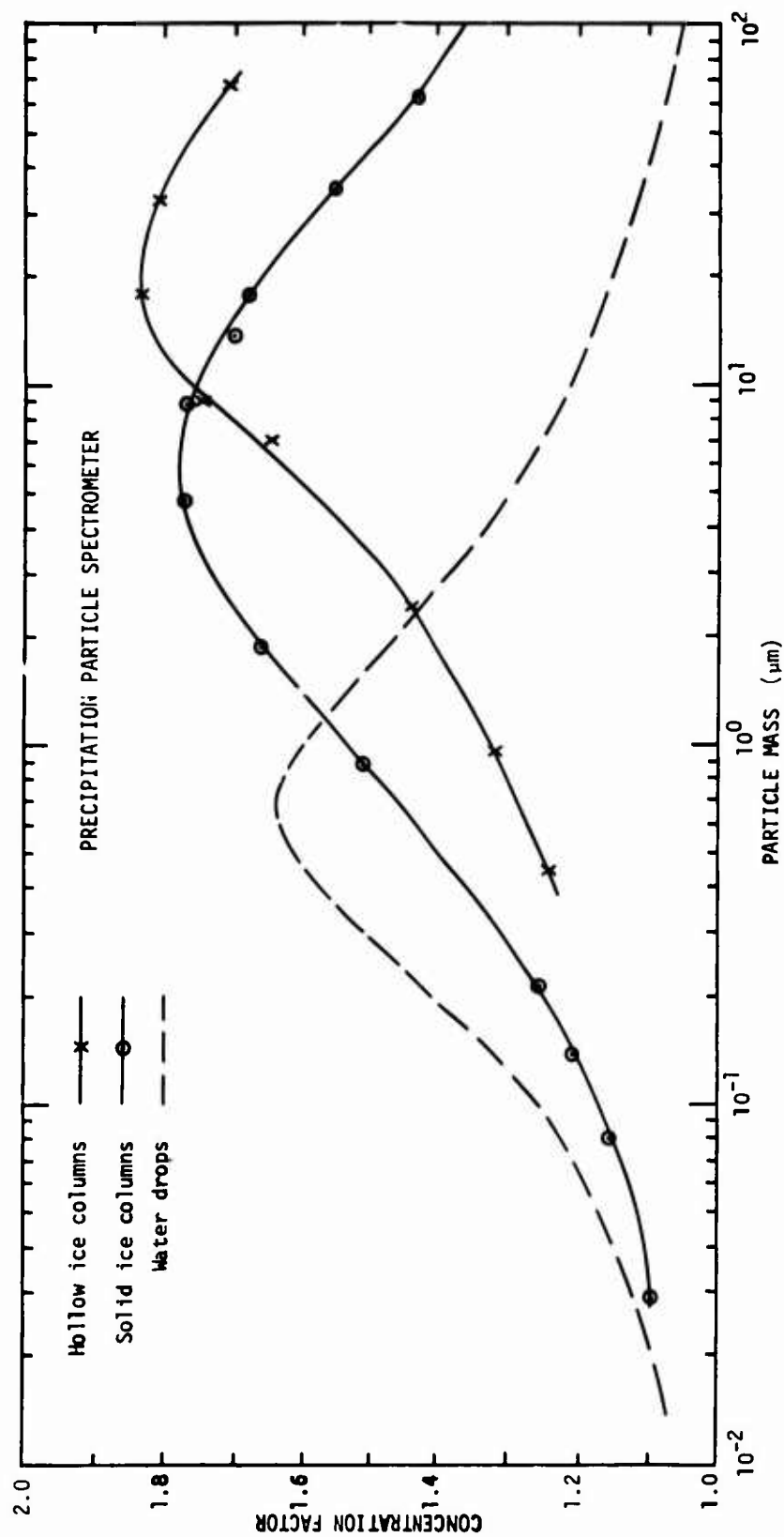


FIGURE 28. Concentration factor vs. particle mass for solid and hollow ice columns at the precipitation particle spectrometer on the Cessna Citation

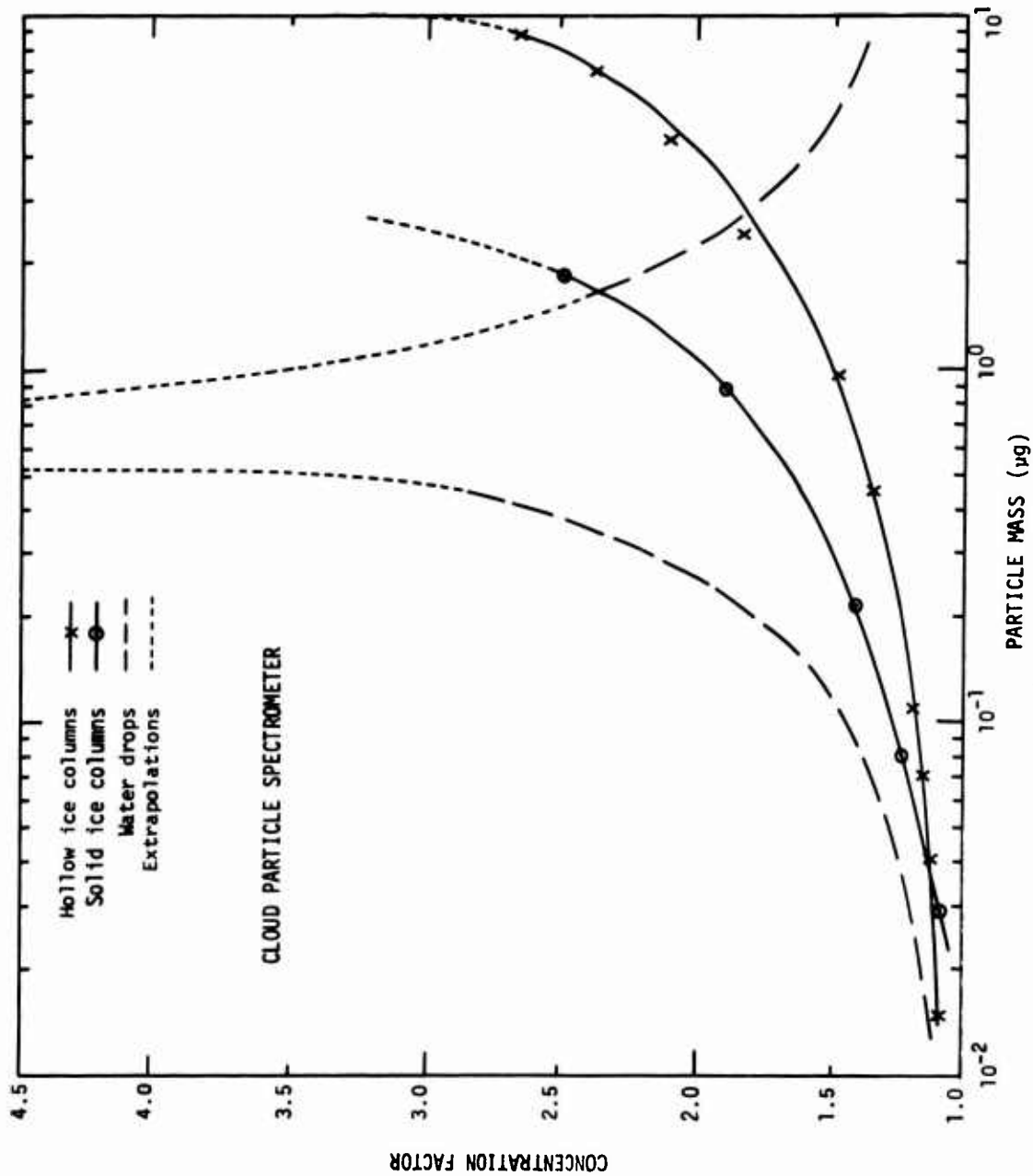


FIGURE 29. Concentration factor vs. particle mass for solid and hollow ice columns at the cloud particle spectrometer on the Cessna Citation

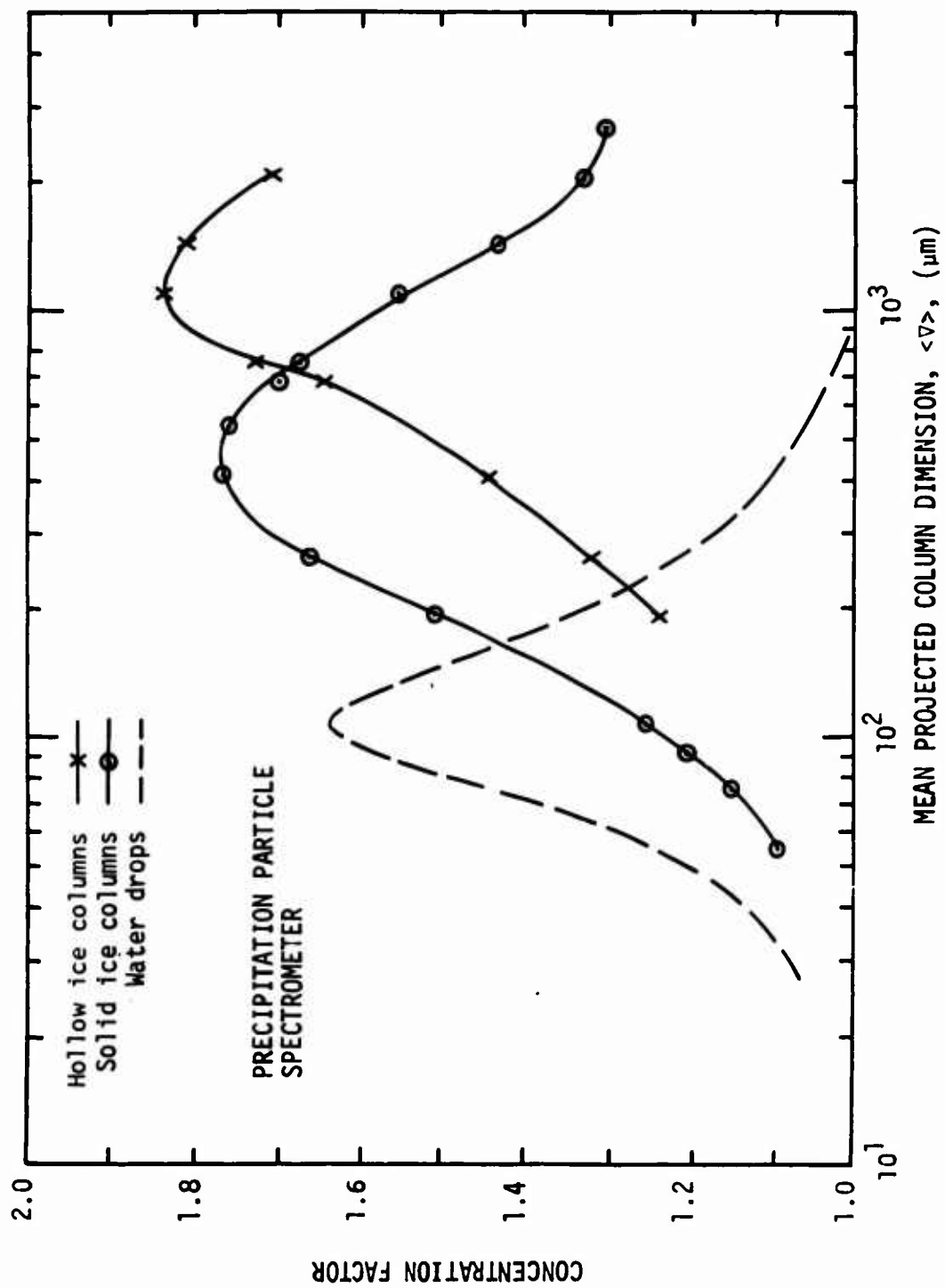


FIGURE 30. Concentration factor vs. mean projected column dimension for solid and hollow ice columns at the precipitation particle spectrometer on the Cessna Citation

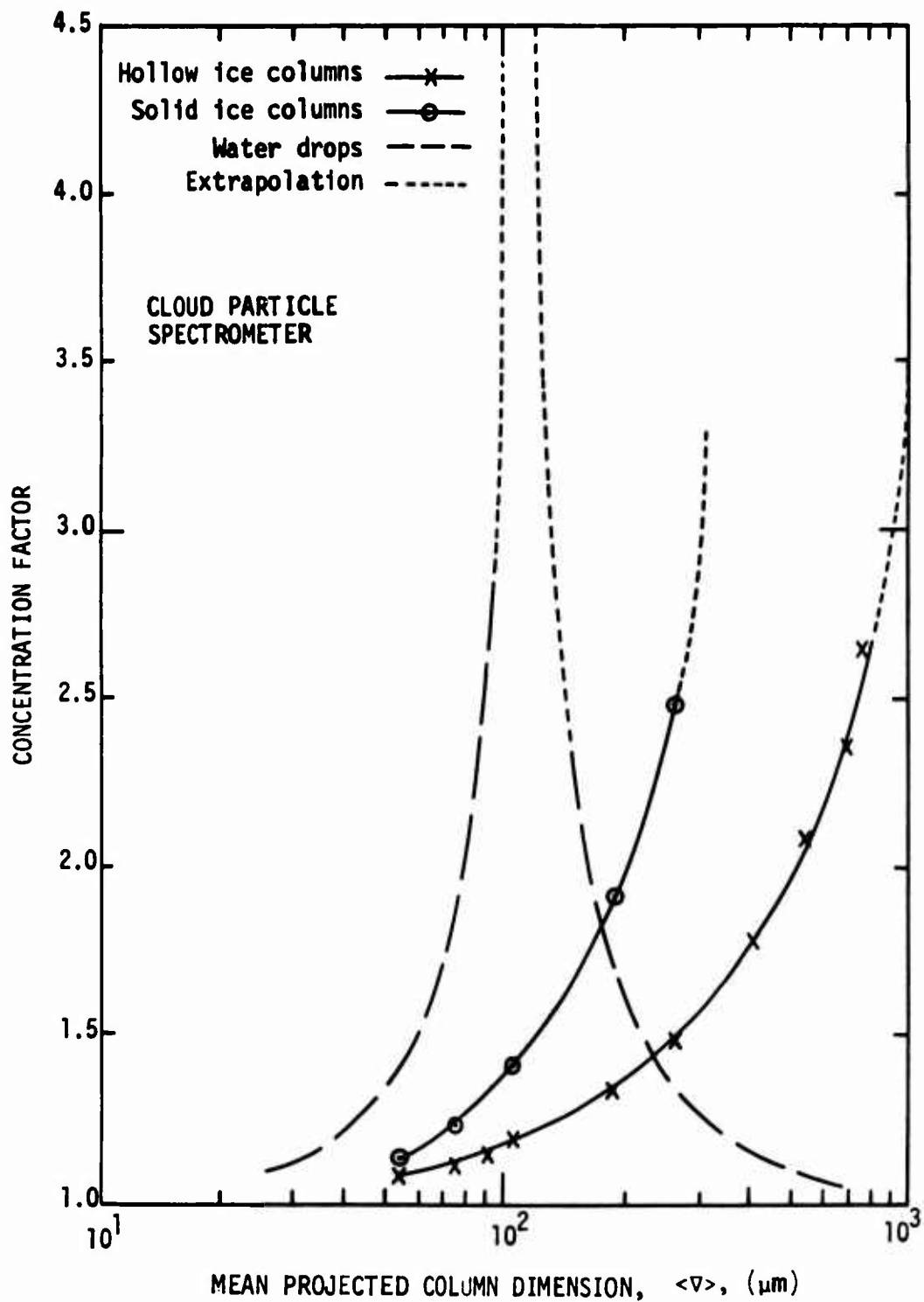


FIGURE 31. Concentration factor vs. mean projected column dimension for solid and hollow ice columns at the cloud particle spectrometer on the Cessna Citation.

TABLE 9

CONCENTRATION FACTORS FOR ICE COLUMNS AT THE KNOLLENBERG
SPECTROMETERS ON THE CESSNA CITATION
(see Tables 1 and 3)

Length, ℓ (μm)	Width, δ (μm)	Concentration Factors			
		Precipitation Particle Spectrometer		Cloud Particle Spectrometer	
		Hollow	Solid	Hollow	Solid
50	35.75		1.09	1.08	1.13
70	50.19		1.15	1.12	1.23
85	59.76		1.21	1.15	
100	68.3		1.25	1.19	1.41
200	98.4	1.24	1.51	1.34	1.90
300	117.0	1.32	1.66	1.48	2.48
500	144.5	1.44	1.76	1.78	
700	165.9		1.76	2.09	
900	183.6	1.65	1.70	2.36	
1000	197.3	1.75	1.68	2.65	
1500	226.5	1.84	1.55		
2000	262.8	1.81	1.43		
3000	310.9	1.71	1.33		
4000	223.1		1.31		



FIGURE 32a. Stereographic plots of four-trajectory, 150 μm -diameter water drop flux tubes to the Cessna Citation cloud particle spectrometer (upper, $C_F = 2.29$) and precipitation particle spectrometer (lower, $C_F = 1.48$). Individual trajectories are not resolved.

$$r_w = .002, \epsilon = .2.$$

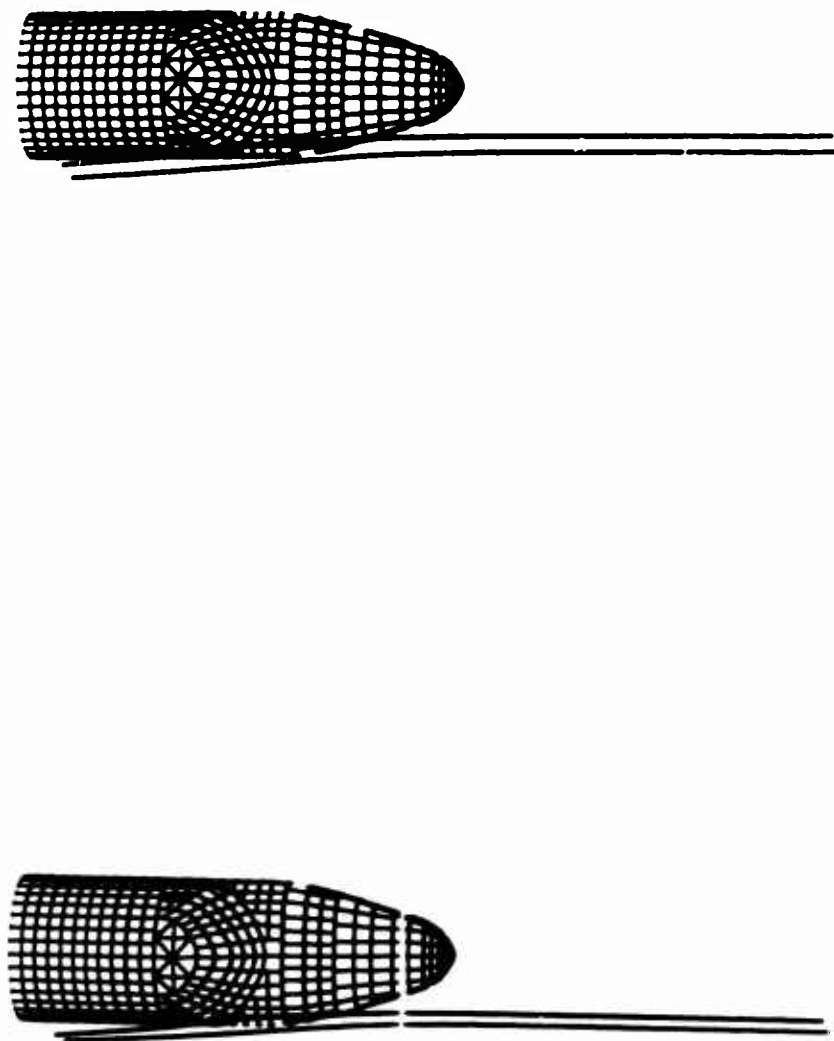


FIGURE 32b. Stereographic plots of four-trajectory, 150 μm -diameter water drop flux tubes to the Cessna Citation cloud particle spectrometer (upper, $C_F = 2.29$) and precipitation particle spectrometer (lower, $C_F = 1.48$). Individual trajectories are not resolved.

$$r_w = .002, \quad \epsilon = .2.$$

ACCURACY OF THE METHOD

NUMERICAL INTEGRATION

Equations (13) are integrated numerically, as an initial value problem, via the code DVDQ of Krogh⁽¹⁷⁾. DVDQ uses a variable time step, variable order, Adams predictor-corrector algorithm. The code has the advantage, which is very important for this application (see p. 23), that it minimizes the number of function evaluations (i.e., air velocity calculations⁽¹⁸⁾).

Small Particles

A sufficiently small particle should essentially follow a streamline since both gravity and inertia effects are negligible. Thus to check the numerical integration accuracy we computed trajectories of 1 μm diameter water drops in axisymmetric flow about a prolate ellipsoid of fineness ratio 2 (see Fig. 3). Streamfunction values were compared at the initial (upstream) particle locations and at the points where the trajectories crossed the extended minor axis of the ellipsoid. By use of the streamfunction gradient along the extended minor axis, we determined that the maximum discrepancy in the axis intersection points is 0.006%. This is for the trajectory closest to the ellipsoid surface. (On the scale of the C130A this represents a trajectory error of 0.28 mm.) Thus, the 1 μm water drops do essentially follow the streamlines. In fact, Fig. 3 is actually a plot of the 1 μm drop trajectories used for this analysis.

Large Particles

Unfortunately there are no theoretical means nor adequate data to check our calculations for large particles. The best that can be done is compare our calculations with those of others. Of the results available in the literature we choose those of Dorsch, Brun, and Gregg⁽¹²⁾ as being the most useful for our purposes. They report

detailed results of calculations of impaction of water drops on prolate ellipsoids of fineness ratio 5. In our studies, we find that calculation of tangent trajectories is quite sensitive to many physical and numerical parameters employed in the computations. Thus we have calculated tangent trajectories and compared them with values given in Fig. 4 of NACA TN-3099.

Dorsch et al. ignore gravity in their calculations. With this simplification we have axial symmetry, and Eqs. (13) become

$$\begin{aligned}\frac{v_{px}}{d\tau} &= \frac{1}{48S_N} (v_{fx} - v_{px}) P \\ \frac{v_{pr}}{d\tau} &= \frac{1}{48S_N} (v_{fr} - v_{pr}) P\end{aligned}\quad (19)$$

where x and r are the axial and radial coordinates, P is the ratio of Best to Reynolds numbers (Eq. (14)), and S_N , variously called: inertial, impaction, or Stokes number, is

$$S_N = \frac{2}{9} \frac{\rho_p (\delta/2)^2 V}{\eta (2L)} = \frac{\rho_p \delta^2 V}{36\eta L} \quad (20)$$

Here S_N is defined to be consistent with Dorsch et al.

A tangent trajectory grazes the body surface. For an axially symmetric case, any trajectory with initial r smaller than r_{tan} , will impact on the body. For fixed body geometry, r_{tan} is a function of the Stokes number, S_N , and a Reynolds number, $R_{N,0}$,

$$R_{N,0} = \frac{\rho V \delta}{\eta} \quad (21)$$

Calculations were done for two sets of S_N , $R_{N,0}$. Results are shown in Table 10. Considering the difference in computational approach (the NACA people used a mechanical differential analyzer), and difference in drag data, agreement is good.

TABLE 10
COMPARISON OF TANGENT TRAJECTORY RESULTS
WITH THOSE OF DORSCH ET AL.⁽¹²⁾

S_N	$R_{N,0}$	r_{tan}	
		<u>Dorsch et al.⁽¹²⁾</u>	<u>Norment and Zalosh</u>
1	4096	.076 ± .0014	.0750 ± .0001
1/30	512	.0200 ± .003	.0150 ± .0001

POTENTIAL FLOW CALCULATIONS

It is well established that potential flow calculations provide excellent approximations to airflow around smooth bodies at subsonic speeds, provided that the skin friction boundary layer and regions of separated flow are avoided. Whitten⁽³⁷⁾ computed the boundary layer thickness on the C130A fuselage; as far aft as FS 350", he found that the boundary layer is no thicker than 3½ inches. Since our target points are greater than 9" away from the fuselage, boundary layer effects do not appear to be significant.

Hess and Smith provide ample proof, in terms of point-by-point comparisons of results, that their method for arbitrary three-dimensional bodies is very accurate^(19,20). We have compared complete

37. R. P. Whitten, "An Investigation of Some Aerodynamic Factors Affecting Meteorological Instrument Readings on a C130A Research Aircraft," Allied Research Associates, AFRD TN-6C-454 (15 May 1960).

trajectories for particles in analytical potential flow about an ellipsoid, with potential flow about a Hess-Smith approximate ellipsoid consisting of 1800 quadrilateral panels. A fineness ratio of 2, which provides a reasonable likeness to the C130A fuselage, was used. Air speed, scale, and air properties were as given in Table 1 for the C130A at 5 kft altitude. Results are shown in Fig. 33 for comparison of trajectory intersections with the extended minor axis. All of the Hess-Smith calculation points are slightly greater than the analytical points. The discrepancies are of acceptable magnitude. The largest discrepancy, for 100 μ m drops at 31 cm, is very atypical in that this point is on the edge of a shadow zone, where: trajectory distortions are near their maxima, concentration factors become very large, and we expect and find "pathological" computational results caused by trajectories crossing each other in this region of extremely high concentration gradients.

AERODYNAMIC PARTICLE DRAG

Drag data for terminal settling of particles are known with high accuracy. Here the question of accuracy arises from use of these data for accelerated motion. No rigorous theory exists for accelerated motion of particles at intermediate and large Reynolds numbers (i.e., beyond the Stokes range). In spite of this, calculations of the kind required here are routinely done. Fuchs discusses this situation in his book⁽⁶⁾. He reasons that as long as the Reynolds number does not exceed several hundred, acceptable results should be obtained by use of steady-state drag coefficients.

It is apparent that for non-steady motion the drag coefficient should be a function of acceleration as well as Reynolds number. Unfortunately, there is considerable confusion in the available experimental data. Fuchs⁽⁶⁾ is of the opinion that the drag should increase relative to the steady state for accelerating motion, but decrease for

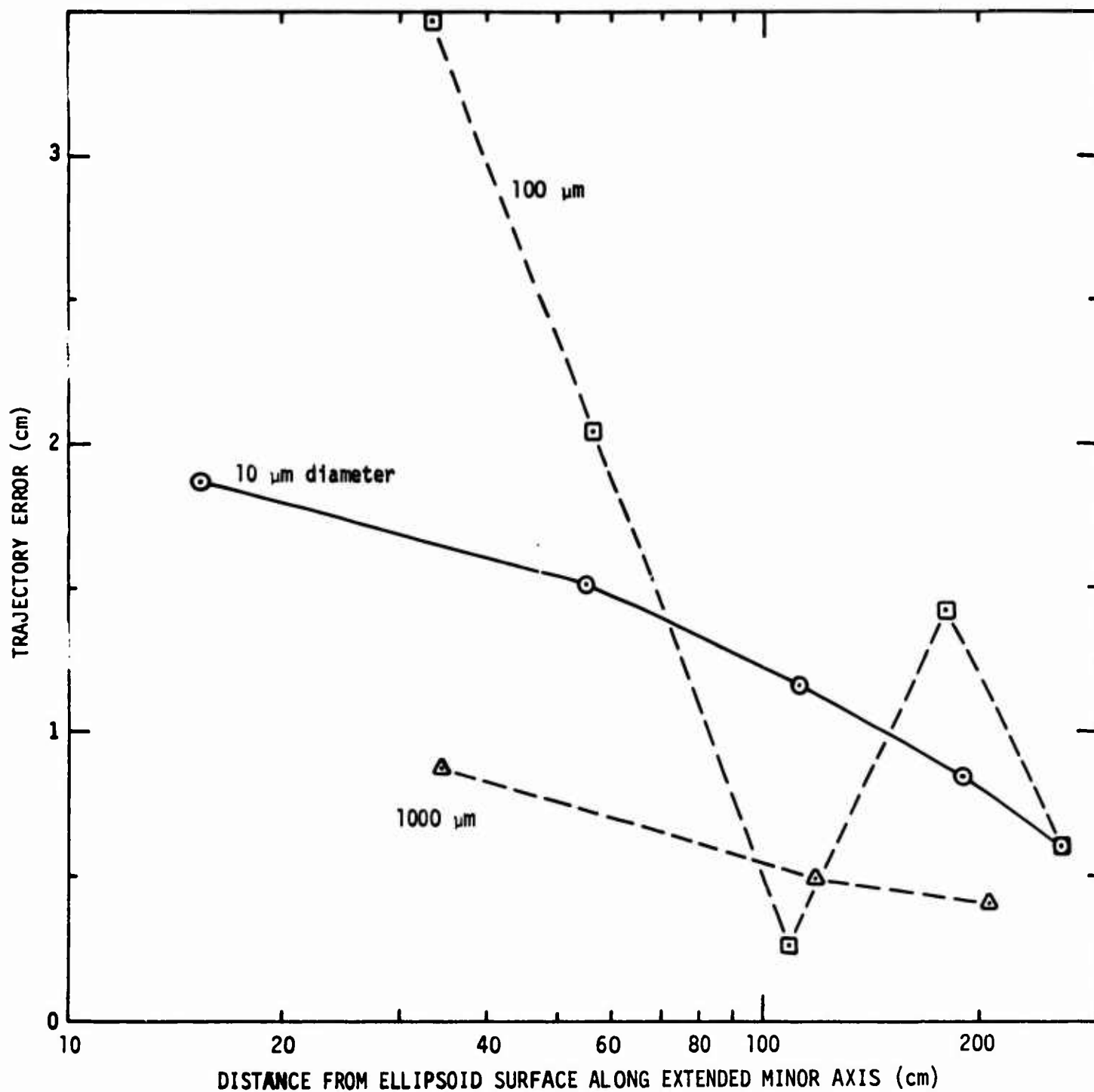


FIGURE 33. Comparison of water drop trajectories about an ellipsoid of fineness ratio 2 using exact and approximate potential airflow. (See text.)

decelerating motion. However, Ingebo⁽³⁸⁾ finds a decreased drag for accelerating motion. Ogden and Jayaweera⁽³⁹⁾ recently found decreased drag for decelerating motion, though less in magnitude than found by Ingebo.

Ingebo's data for spheres very nicely fit a power law relation between C_D and R_N . His relation is

$$C_D = 27 R_N^{-0.84} . \quad (22)$$

Notice the independence of acceleration. Equation (22) can be compared with Stokes law, which it should approach in the limit as $R_N \rightarrow 0$,

$$C_D = 24 R_N^{-1} , \quad (23)$$

and to an approximation equation for terminal settling of spheres at large Reynolds numbers,

$$C_D = 28 R_N^{-0.85} + 0.48 . \quad (24)$$

We have performed some exploratory calculations to assess the effect of non-steady motion on concentration factor calculations. These calculations consist of two kinds. First, we subject initially steady-settling water drops to an impulsive onset of air flow, and compute the drop response using (a) steady-state drag coefficients, and (b) Ingebo

38. R. D. Ingebo, "Drag Coefficients for Droplets and Solid Spheres in Clouds Accelerating in Airstreams," NACA-TN 3762 (Sept. 1956).

39. T. L. Ogden and K. O. L. F. Jayaweera, "Drag Coefficients of Water Drops Decelerating in Air," Quart. J. Roy. Met. Soc. 97, 571 (1971).

drag coefficients*. Results, in terms of relaxation time**, are shown in Fig. 34 for the horizontal velocity component after impulsive onset of a 1 m/sec air velocity in the horizontal direction. There is little difference for the small drops, but progressively greater difference as the drop size increases. Air temperature and density are as given in Table 1 for 5 kft altitude. Second, we computed concentration factors for a few representative cases. Results are shown in Table 11. These calculations indicate the possibility of a significant effect. In any case, this problem needs additional study because of the lack of a sound basis for use of the steady-state drag coefficients for accelerative motion.

TABLE 11

COMPARISON OF STEADY-STATE AND INGEBO DRAG CONCENTRATION FACTORS
AT THE PARTICLE REPLICATOR SLIT ON THE LOCKHEED C130A

(Conditions are as given in Table 1 for 5 kft altitude)

Water drop diameter (μm)	Concentration Factors	
	Steady State	Ingebo
100	1.40	1.24
150	1.33	1.10

* Numerical problems arise when Ingebo's relation is used at very low Reynolds numbers. Therefore, we switch over to Stokes' relation where the Stokes and Ingebo curves cross, at $R_N = 0.47896$.

** Relaxation time is time required for a particle to reach $1-1/e$ of its final velocity.

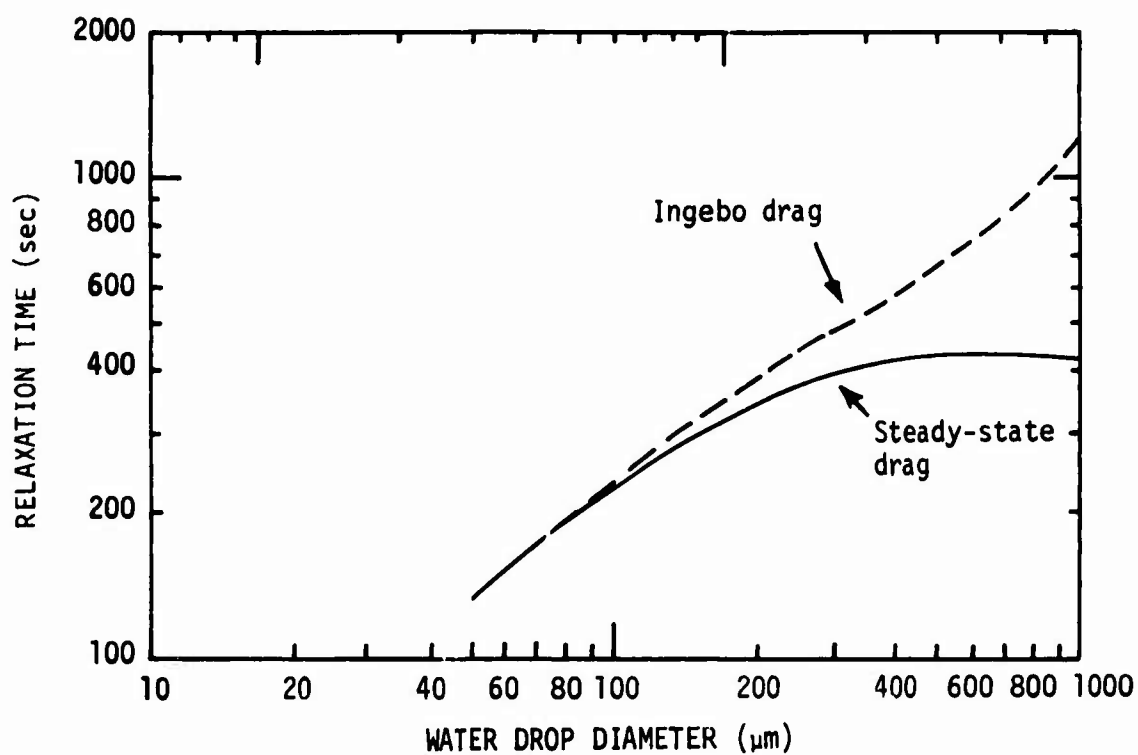


FIGURE 34. Relaxation times of water drops, computed by steady-state and Ingebo drag coefficients, in response to a 1 m/sec impulsive horizontal flow.

SENSITIVITY TO FLUX TUBE STRUCTURE

It might be supposed that concentration factor accuracy is sensitive to the structure of the particle flux tube, since the flux tube is used to approximate an infinitesimal property of the flow. Accordingly, sensitivity studies were done for water drops at the C130A particle replicator at 5 kft altitude. Results are shown in Table 12. Over a wide range of tube structures, maximum differences of less than 2% are found. These differences are no greater than those found with the same tube structure, but with different initialization guesses.

PARTICLE SHAPE AND ORIENTATION

We assume spherical shape for water drops. This simplification is consistent with the observation of negligible shape deformation for terminally settling drops smaller than $\sim 400 \mu\text{m}$ diameter. Furthermore, the smaller drops are not expected to deform appreciably in the weak shear found outside the boundary layer. Since concentration factors approach unity for drops larger than $400 \mu\text{m}$, we conclude that for water drops we have neither a shape nor orientation problem.

For ice columns we have computed concentration factors for "axis-on" and "end-on" column orientations relative to the drag vector (see Fig. 10). Many have observed that the "axis-on" orientation is preferred, and Bragg et al.⁽³⁴⁾ observe that this orientation is very rapidly attained. Thus, for well formed, unrimed ice columns, our "axis-on" concentration factor results can be accepted with confidence. On the other hand, fragmented or rimed columns tend to oscillate, tumble, or, in extreme cases, settle with their long axes oriented vertically. Our results may not be representative for such cases.

As yet we have not applied our method to other ice forms: plates, aggregates, dendrites, etc. It will be interesting to see how results for these forms compare with results for drops and columns.

TABLE 12

SENSITIVITY OF C_F TO FLUX TUBE STRUCTURE

100 μ m Water Drops at the C130A Replicator Slit
5 kft altitude

A. Number of Trajectories on the Tube Surface ($r_w = .01$, $\epsilon = .2$)

<u>N</u>	<u>C_F</u>
4	1.399
6	1.388
8	1.391

B. Target Window Radius and Convergence Tolerance

<u>ϵ</u>	$r_w =$	<u>C_F</u>		
		<u>.005</u>	<u>.01</u>	<u>.02</u>
0.05		1.390		1.413
0.1			1.394	
0.2		1.393		1.412
0.4			1.400	

SUMMARY AND DISCUSSION

We are satisfied that integration and flow calculation numerical errors are negligible. The digital descriptions of the Lockheed airplane fuselages are very accurate (~ 0.02 inch). For the Cessna, some interpolation was necessary, but individual coordinates are known to better than $2\frac{1}{2}$ -inch accuracy. Provided that the skin friction boundary layer and regions of separated flow are avoided, the potential flow calculations yield accurate simulation of the air flow. Steady-state drag for spheres and columns is accurately known, well beyond the range of Reynolds numbers encountered (Appendix B).

For water drops, the only major source of error appears to be use of the steady drag data for accelerative motion. Sensitivity results presented above (i.e., comparisons of steady drag results with results using Ingebo's drag data) would appear to overstate the error in light of the results of Ogden and Jayaweera⁽³⁹⁾. We conclude that concentration factor errors for water drops are less than 20%, except near the edge of a shadow zone. We suggest use of the method presented here to correct existing data.

For ice, the situation is much more complex. On the basis of the error analyses above, and the results presented in the preceding chapter, we might claim an accuracy of 30-40% for columns. On the other hand, there are a number of uncertainties that are essentially beyond our control. For example, our results strictly apply only to well formed, unrimed ice crystals. We have used typical column dimensions and densities, but these properties of ice crystals are observed to vary widely. For the Knollenberg spectrometers, the question of how to relate instrument-registered ice particle dimensions with true particle shape, dimensions, and density is an open one. We must defer assignment of a quantitative error estimate until other crystal forms are studied.

CONCLUSIONS

A method has been developed to compute concentration distortion of particulates of arbitrary size caused by airflow around airplane fuselages. The method combines a three-dimensional potential airflow solution with three-dimensional hydrometeor trajectories around the airplane. It has been applied to hydrometeor sampling instruments on three cloud physics research airplanes: Lockheed C130A and C130E transports, and a Cessna Citation jet. Results have been obtained for water drops and ice columns.

On a Lockheed C130A a formvar particle replicator mounted just aft of the cockpit was studied. For both water drops and ice columns, substantial concentration enhancement (from 30-60%) over a wide range of particle sizes was found.

On the Lockheed C130E a formvar particle replicator mounted in the forward cargo compartment was studied. At 5 kft altitude, the calculation indicated that water drops over a range from about 90-300 μm diameters cannot be sampled by the instrument. For other drop sizes severe concentration enhancement is indicated. This instrument is being redesigned to extend the sampling point 8 inches further from the fuselage. At the new point the calculations indicate concentration enhancement (up to 40%) over a substantial range of sizes.

Knollenberg particle spectrometers mounted on the emergency exit door of the Cessna Citation were studied. At the precipitation particle spectrometer, concentration enhancement (up to 80%) over a wide range of sizes for water drops and ice columns are indicated. For the cloud particle spectrometer, water drops over a narrow range near 100 μm diameter cannot be sampled, nor can ice greater in size than about 300 μm for solid columns and 800 μm for hollow columns. Severe concentration enhancement is indicated for other sizes.

A thorough error analysis indicates concentration factor accuracy of $\sim 20\%$ for water drops. We suggest use of the method to correct existing water drop data. Accuracy assessment of ice particle results is deferred until additional crystal forms are studied.

APPENDIX A. ITERATIVE PROCEDURES TO DETERMINE THE PARTICLE TRAJECTORY THROUGH A POINT IN SPACE

If the flow field is so complicated that particle trajectories must be calculated numerically, the particle velocity through a point must be known to determine the particle trajectory through that point. Since in this work we do not have a priori knowledge of particle velocities at target points, we cannot determine trajectories by backward calculation in time. Instead, we must begin at a point far upstream where the particle velocity is known, and calculate forward in time. Since we also do not have a priori knowledge of the initial point of the desired trajectory, the trajectory must be determined by a trial-and-error iterative process. The theory is given in the Concentration Factor section (p. 13). Here, we develop the detailed equations and describe their application.

Our fundamental equation is a first order approximation to a Taylor's series that relates coordinate points in the initial and target planes, i.e., planes perpendicular to the particle velocity vector far upstream and at the target. Let our target point be $Z_{t,0}$, and Z_t be an arbitrary point in the target plane which is close to $Z_{t,0}$. Let Z be the point of intersection in the initial plane of the particle trajectory through Z_t . Our fundamental equation is

$$Z = B + C(Z_t - Z_{t,0}) \quad , \quad (A-1)$$

where all quantities are complex, e.g., $Z_t = \zeta_t + i\xi_t$ and $B = b_\zeta + ib_\xi$. (ζ_t and ξ_t denote the Cartesian coordinates of a point in the target plane).

We are given $Z_{t,0}$ and we begin our iterative procedure by guessing two sets of values for Z_t and Z , which we label $Z_{t,1}$, Z_1 and $Z_{t,2}$, Z_2 . In terms of the real and imaginary parts of Eq. (A-1) these points yield four simultaneous equations in the four unknowns, b_ζ , b_ξ , c_ζ , c_ξ which in matrix notation is

$$\begin{bmatrix} 1 & 0 & \Delta\zeta_{t,1} & -\Delta\xi_{t,1} \\ 0 & 1 & \Delta\xi_{t,1} & \Delta\zeta_{t,1} \\ 1 & 0 & \Delta\zeta_{t,2} & -\Delta\xi_{t,2} \\ 0 & 1 & \Delta\xi_{t,2} & \Delta\zeta_{t,2} \end{bmatrix} \cdot \begin{bmatrix} b_\zeta \\ b_\xi \\ c_\zeta \\ c_\xi \end{bmatrix} = \begin{bmatrix} \zeta_1 \\ \xi_1 \\ \zeta_2 \\ \xi_2 \end{bmatrix} \quad (\text{A-2})$$

where $\Delta\zeta_{t,1} = \zeta_{t,1} - \zeta_{t,0}$, $\Delta\xi_{t,1} = \xi_{t,1} - \xi_{t,0}$, etc. This system of equations is solved for b_ζ and b_ξ , which, as seen from Eq. (A-1), provide the next estimate of the desired initial coordinates Z . Using these initial coordinates, which we label Z_3 , a trajectory is computed and the corresponding $Z_{t,3}$ is determined. Then we repeat the matrix inversion using

$$Z_2 = B + C\Delta Z_{t,2}$$

$$Z_3 = B + C\Delta Z_{t,3}$$

and determine a revised B , and so on.

This procedure works well but it uses only the most recent two sets of results. If the method has not converged after calculation of two trajectories, we switch over to a least squares procedure which uses all trajectory data that have been generated. The real and imaginary parts of Eq. (A-1) are

$$\zeta = b_\zeta + c_\zeta \Delta\zeta_t - c_\xi \Delta\xi_t \quad (\text{A-3})$$

$$\xi = b_\xi + c_\zeta \Delta\xi_t + c_\xi \Delta\zeta_t$$

After eliminating the term in c_ξ , we obtain

$$R = b_{\zeta} \Delta \zeta_t + b_{\xi} \Delta \xi_t + c_{\zeta} |\Delta Z_t|^2 \quad (\text{A-4})$$

where

$$R = \Delta \zeta_t \zeta + \Delta \xi_t \xi \quad (\text{A-5})$$

b_{ζ} , b_{ξ} , and c_{ζ} are determined such that

$$\sum \left(R - b_{\zeta} \Delta \zeta_t - b_{\xi} \Delta \xi_t - c_{\zeta} |\Delta Z_t|^2 \right)^2$$

is minimized, where the summation is over all of the trajectory results. The normal equations matrix is

$$\begin{bmatrix} \sum (\Delta \zeta_t)^2 & \sum \Delta \zeta_t \Delta \xi_t & \sum \Delta \zeta_t |\Delta Z_t|^2 \\ \sum (\Delta \xi_t)^2 & \sum \Delta \xi_t |\Delta Z_t|^2 & \\ \sum (|\Delta Z_t|^2)^2 & & \end{bmatrix} \cdot \begin{bmatrix} b_{\zeta} \\ b_{\xi} \\ c_{\zeta} \end{bmatrix} = \begin{bmatrix} \sum \Delta \zeta_t R \\ \sum \Delta \xi_t R \\ \sum |\Delta Z_t|^2 R \end{bmatrix} \quad (\text{A-6})$$

Iteration is continued until the current Z_t , labeled $Z_{t,j}$, is within a prescribed tolerance (Eq. (11)) of being equal to $Z_{t,0}$.

In an effort to improve convergence efficiency, a second-order version of the iteration procedure was tried. Our fundamental equation becomes

$$Z = B + C(Z_t - Z_{t,0}) + D(Z_t - Z_{t,0})^2 \quad (\text{A-7})$$

This yielded no improvement in convergence, and was abandoned in favor of the simpler first order method.

A code has been developed that performs automatically the calculations required to determine a concentration factor. The code is supplied with flight conditions and the output of the Hess-Smith code so that velocities at arbitrary points in space can be computed. In addition, it is given the target point coordinates, the target plane window radius, r_w , the tolerance, ϵ , the number of trajectories to be used to define the flux tube, and two sets of initial and target plane coordinates. The code first finds the trajectory through the central target point by iteration until Eq. (11) is satisfied. (In the event that convergence is not achieved in 25 attempts the concentration factor calculation is abandoned.) Then it finds each of the flux tube trajectories in a similar manner. It computes the areas of the polygons defined by the trajectory intersections in the initial and target planes, and computes the concentration factor as the ratio of the areas.

In the course of the iterative calculations, impaction on the airplane body frequently occurs. In this event the initial coordinates, ζ , ξ , are incremented by 1% of their values such as to shift the trajectory away from the body, and the calculation is begun again. If a total of 25 impactions are registered in attempting to compute the trajectory through a target point, the concentration factor calculation is abandoned.

APPENDIX B. AERODYNAMIC DRAG ON MOVING PARTICLES

GENERAL CONSIDERATIONS

In this work, we take particle motion relative to the air to result from two phenomena: (1) free-fall, gravity settling, and (2) particle inertia relative to air being displaced by a passing air-plane. Turbulence effects are unimportant over the time intervals considered here.

An adequate data base exists to allow accurate calculation of terminal settling of particles of simple shapes. For accelerative motion of particles, there are neither adequate data nor theory. Nevertheless, we use the terminal settling drag data for accelerative motion computations. This situation is discussed in the chapter on Accuracy.

It is easy to show from Eq. (12) that the Best number for terminal particle settling, $B_{N,T}$ ($= R_{N,T}^2 C_D$), is

$$B_{N,T} = \frac{2\rho\delta^2mg}{\eta^2A_p} \quad . \quad (B-1)$$

Symbols are as defined previously (also see Appendix D). Notice that $B_{N,T}$ is independent of the particle settling speed. Since $B_{N,T}$ is a function of all of the particle and fluid properties that determine flow around the particle, the settling speed must be a function of $B_{N,T}$. Thus

$$R_{N,T} = f_1(B_{N,T}) \quad , \quad (B-2)$$

where $R_{N,T}$, the Reynolds number for terminal settling is

$$R_{N,T} = \frac{\rho V_T \delta}{\eta} \quad . \quad (B-3)$$

Data needed to determine $f_1(B_{N,T})$ are available in the literature, and are discussed below.

In computing particle trajectories through complex flow fields, we integrate Eqs. (13) numerically, step-by-step forward in time. At any time, and corresponding point in space, the particle Reynolds number is known. We must determine $P = B_N/R_N$ from the Reynolds number. For this purpose, we use the same data as is used to determine function $f_1(B_{N,T})$, but in reverse order, to determine the function, f_2

$$B_N = f_2(R_N) \quad . \quad (B-4)$$

As noted previously, f_2 should be a function of acceleration as well as Reynolds number, but for moderate Reynolds numbers and accelerations Eq. (B-4) seems to yield an adequate approximation.

In the remainder of this Appendix, we discuss our determinations of the functions f_1 and f_2 .

SPHERES

The Best number for terminal settling of spheres reduces to

$$B_{N,T} = \frac{4}{3} \frac{\rho_p \delta^3 g}{\eta} \quad (B-5)$$

where ρ_p is sphere density. Davies⁽⁴⁰⁾ fits the following functions to a large body of experimental data:

40. C. N. Davies, "Definitive Equations for the Fluid Resistance of Spheres," Proc. Phys. Soc (London) 57, 259 (1945).

$$R_{N,T} = \frac{B_{N,T}}{24} - 2.3363 \times 10^{-4} B_{N,T}^2 + 2.0154 \times 10^{-6} B_{N,T}^3 - 6.9105 \times 10^{-9} B_{N,T}^4, \quad B_{N,T} \leq 140 \quad (B-6)$$

$$\begin{aligned} \log_{10} R_{N,T} = & -1.29536 + 0.986 (\log_{10} B_{N,T}) \\ & - 0.046677 (\log_{10} B_{N,T})^2 \\ & + 0.0011235 (\log_{10} B_{N,T})^3, \\ & 100 < B_{N,T} \leq 4.5 \times 10^7 \end{aligned} \quad (B-7)$$

To find f_2 , we have fit the data tabulated by Davies to polynomials in $R_{N,T}$, viz.

$$B_N = \sum_{j=0}^n a_j R_N^j. \quad (B-8)$$

The polynomial coefficients determined by least squares are given in Table 13.

TABLE 13

POLYNOMIAL COEFFICIENTS RELATING BEST NUMBER
TO REYNOLDS NUMBER FOR SPHERES

$$B_N = \sum_{j=0}^n a_j R_N^j$$

<u>Reynolds No. Range</u>	<u>j</u>	<u>a_j</u>
0.05 < R _N ≤ 3	0	0
	1	24.167
	2	3.2540
	3	-0.23564
3 < R _N ≤ 330	0	-28.339
	1	38.969
	2	0.73204
	3	-0.00056084
330 < R _N	0	0
	1	93.462
	2	0.37576

COLUMNS

Experimental data for "axis-on", terminal settling of cylinders is reported by Kajikawa⁽⁴¹⁾, Jayaweera and Mason⁽³³⁾, and Jayaweera and Cottis⁽⁴²⁾. Though these data are for circular based cylinders, Jayaweera and Cottis⁽⁴²⁾ maintain that they can be used for hexagonal based cylinders without significant error. For terminal setting, the Best number is

$$B_{N,T} = \frac{2mg\rho}{\eta} \frac{\delta}{\ell} \quad (B-9)$$

where δ and ℓ are as defined in Fig. 10, and the Reynolds number is

$$R_{N,T} = \frac{\rho\delta V_T}{\eta} \quad (B-10)$$

By use of a Kargel Reflecting Projector, we transferred the graphically displayed data points of Kajikawa and Jayaweera and Cottis to lined graph paper. Each datum was independently recorded at least twice. With two exceptions these authors made their measurements for the same δ/ℓ values. The data set for one exceptional δ/ℓ (0.2) is inconsistent with the remainder and was discarded. Data for $\delta/\ell=0$, measured by Jayaweera and Mason⁽³³⁾, were taken from the presentation of Jayaweera and Cottis. The data from the two papers were merged and fitted via least squares to polynomial functions of $\log_{10} (R_{N,T})$ vs. $\log_{10} (B_{N,T})$. These polynomials are described in Table 14. In Table 15 are the least squares coefficients for the inverse polynomials used to evaluate $\log_{10} B_N$ from $\log_{10} R_N$.

-
41. M. Kajikawa, "A Model Experimental Study on the Falling Velocity of Ice Crystals," J. Met. Soc. Japan 49, 367 (1971).
 42. K. O. L. F. Jayaweera and R. E. Cottis. "Fall Velocities of Plate-Like and Columnar Ice Crystals," Quart. J. Roy. Met. Soc. 95, 703 (1969).

TABLE 14

POLYNOMIAL COEFFICIENTS RELATING REYNOLDS NUMBER TO BEST NUMBER
FOR AXIS-ON TERMINAL SETTLING OF CYLINDERS

$$\log_{10} R_{N,T} = \sum_{j=0}^4 b_j (\log_{10} B_{N,T})^j$$

δ/l	b_0	b_1	b_2	b_3	b_4	Number of data points		
						J&C	Kaj	Total
0.0	-.76690	.85642	-.060794	.011948	-.0019287	26	0	26
0.1	-.84486	.87235	-.065890	.013440	-.0018927	20	19	39
0.5	-1.1073	.98200	-.054802	0	0	17	16	33
1.0	-1.3140	1.0115	-.035804	-.0034749	0	21	16	37

δ/l	Range in $R_{N,T}$	Range in $B_{N,T}$
0.0	.188 - 84	1.11 - 8400
0.1	.0219 - 71	.136 - 630
0.5	.00664 - 107	.090 - 12600
1.0	.00398 - 98	.088 - 12300

TABLE 15

POLYNOMIAL COEFFICIENTS RELATING BEST NUMBER TO REYNOLDS NUMBER
FOR AXIS-ON CYLINDER DRAG

$$\log_{10} B_N = \sum_{j=0}^4 a_j [\log_{10} R_N]^j$$

δ/l	a_0	a_1	a_2	a_3	a_4
0.0	.95007	1.3137	.073827	-.023087	.024530
0.1	1.0320	1.2841	.090954	.0064871	0
0.5	1.2048	1.1746	.10077	.015304	0
1.0	1.3679	1.1124	.087279	.018643	0

Kajikawa⁽⁴¹⁾ gives data for "end-on" terminal settling of columns. As noted previously, we have good reason to reject this settling orientation for ice columns in the free air. On the other hand, there is some probability, albeit small, that columns will orient with their axes parallel with the drag vector. Therefore, we have reduced Kajikawa's end-on drag data as described above to yield the polynomials given in Table 16. Concentration factor results shown in Figs. 15-18 and tabulated in Table 6 for end-on column orientation were computed using these polynomials. They were used to compute drag on the columns during the trajectory calculations, though settling was computed via use of the axis-on polynomials.

TABLE 16

POLYNOMIAL COEFFICIENTS RELATING BEST NUMBER TO
REYNOLDS NUMBER FOR END-ON CYLINDER DRAG

$$\log_{10} B_N = \sum_{j=0}^2 a_j (\log_{10} R_N)^j$$

δ/l	a_0	a_1	a_2	Number of data points
1/3	1.6098	1.0259	0.0	3
1/2	1.4616	0.99954	0.0	3
1/1	1.4513	1.0724	0.021773	4

APPLICATION OF THE DRAG POLYNOMIALS

Given drop diameter or crystal dimensions, particle density and atmospheric properties, $B_{N,T}$ is calculated by Eq. (B-5) or (B-9). For water drops, $R_{N,T}$ is calculated from Eq. (B-6) or (B-7). For ice columns, $\log_{10} R_{N,T}$ values are calculated via the two polynomials in Table 14 that bracket the given δ/λ value. $\log_{10}(R_{N,T})$ for the column is found by linear interpolation in δ/λ . Finally, V_T is computed as

$$V_T = \frac{\eta R_{N,T}}{\rho \delta} \quad . \quad (B-11)$$

To compute the drag on a particle during integration of the particle equations of motion, a similar procedure is followed. The Reynolds number is computed from Eq. (16). For a water drop, B_N is computed from Eq. (B-8). For ice columns, $\log_{10} B_N$ is computed via the polynomials in Table 15 or 16 that bracket the given δ/λ value. Finally, $\log_{10} B_N$ for the given δ/λ is obtained by linear interpolation in δ/λ .

APPENDIX C. PROJECTED DIMENSION OF RANDOMLY ORIENTED RECTANGLES

Here we wish to relate actual ice column dimensions, δ and ℓ , to the mean characteristic dimension recorded by the Knollenberg spectrometers. We assume that ice columns settle with their long axes at random attitudes in the horizontal plane. A horizontally oriented linear sizing instrument will register a projection of the column dimensions onto its linear axis.

A plan view of the geometry is shown in Fig. C.1, where the long axis of length ℓ makes an angle θ with the projection direction. The short axis has length δ . From the drawing we see that the projected dimension, ∇ , is

$$\nabla = \ell \sin \theta + \delta \cos \theta . \quad (C-1)$$

The probability that θ will assume a value between θ and $\theta + d\theta$ is simply

$$dp(\theta) = \frac{2}{\pi} d\theta , \quad 0 \leq \theta \leq \frac{\pi}{2} . \quad (C-2)$$

Therefore, for fixed ℓ and δ the mean value of ∇ is

$$\begin{aligned} \langle \nabla \rangle &= \int_0^{\pi/2} \nabla dp(\theta) = \frac{2}{\pi} \int_0^{\pi/2} (\ell \sin \theta + \delta \cos \theta) d\theta \\ \langle \nabla \rangle &= \frac{2}{\pi} (\ell + \delta) . \end{aligned} \quad (C-3)$$

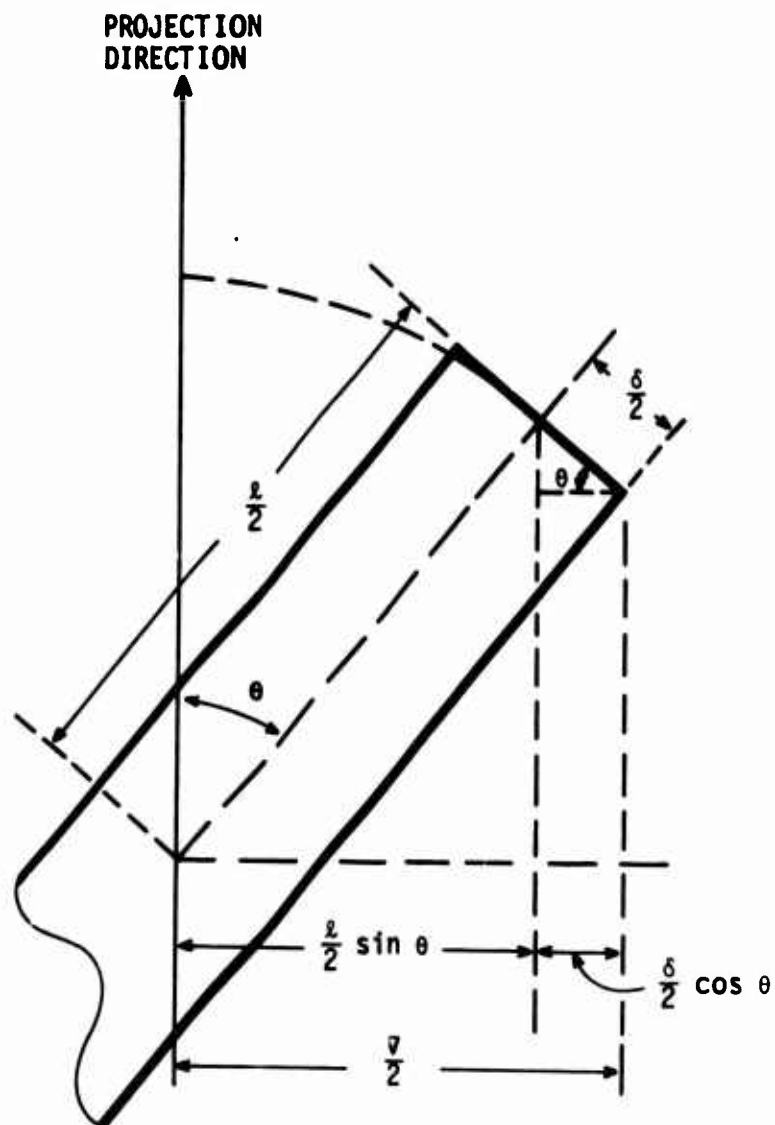


FIGURE C.1. Geometry of a rectangle oriented at angle θ to the projection direction

APPENDIX D. GLOSSARY OF SYMBOLS

A	cross-sectional area of a particle flux tube in the free-stream (m^2)
A_p	area of particle projected in its direction of motion (m^2)
A_t	cross-sectional area of a particle flux tube in the target plane (m^2)
B_N	Best number
BL	coordinate perpendicular to fuselage symmetry axis (English units)
C_D	drag coefficient (dimensionless)
C_F	concentration factor (Eq. (1))
C_M	particle concentration ratio (Eq. (2))
F	particle flux in the free-stream ($kg/(m^2\text{-sec})$)
F_N	Froude number
F_t	particle flux at a target point ($kg/(m^2\text{-sec})$)
FS	coordinate parallel with fuselage axis (English units)
g	gravity acceleration constant (9.8 m/sec^2)
\vec{g}	acceleration of gravity (m/sec^2)
i	$\sqrt{-1}$
λ	ice column length (μm)
L	characteristic dimension of an airplane (m, feet or inches)
m	particle mass (kg)
\dot{M}	mass transfer rate through a particle flux tube (kg/sec)
P	ratio of Best to Reynolds numbers ($P = B_N/R_N$)

P_T	ratio of Best to Reynolds numbers for terminal particle settling
r_w	radius of particle flux tube cross section in the target plane (dimensionless)
R_N	Reynolds number
S_N	Stokes number
t	time (sec)
v_{fx}, v_{fy}, v_{fz}	air velocity components (dimensionless)
v_{px}, v_{py}, v_{pz}	particle velocity components (dimensionless)
v_t	air speed at the target point (dimensionless)
v_T	terminal settling speed of a particle (dimensionless)
V	free-stream air speed (m/sec)
\vec{V}_f	air velocity (m/sec)
\vec{V}_p	particle velocity (m/sec)
V_t	air speed at the target point (m/sec)
V_T	terminal settling speed of a particle (m/sec)
WL	vertical coordinate in fuselage system (English units)
x, y, z	space coordinates (dimensionless)
Z	complex point in a plane perpendicular to a particle flux tube (dimensionless) ($Z = \zeta + i\xi$)
$Z_{t,0}$	target point ($Z_{t,0} = \zeta_{t,0} + i\xi_{t,0}$)
ξ	imaginary coordinate of a complex point in a plane perpendicular to a particle flux tube (dimensionless)
ρ	air density (kg/m^3)
ρ_p	particle density (kg/m^3)

τ	time (dimensionless)
δ	particle dimension (μm). (water drop diameter or column base width)
ϵ	fraction of r_w used for trajectory conversion criterion (see Eq. (11))
ζ	real coordinate of a complex point in a plane perpendicular to a particle flux tube (dimensionless)
η	air viscosity (kg/(m-sec))
∇	projected dimension of an ice column (μm)

REFERENCES

1. P. Spyers-Duran and R. R. Braham, "An Airborne Continuous Cloud Particle Replicator," *J. Appl. Meteor.* 6, 1108 (1967).
2. J. Hallett, R. W. Hanaway, and P. B. Wagner, "Design and Construction of a New Cloud Particle Replicator for Use on a Pressurized Aircraft," Desert Research Institute, Reno, Nevada, AFCRL-72-0410 (31 May 1972). AD-753 091.
3. R. G. Knollenberg, "The Optical Array: An Alternative to Scattering or Extinction for Airborne Particle Size Determination," *J. Appl. Meteor.* 9, 86 (1970).
4. R. G. Dorsch and R. J. Brun, "Variation of Local Liquid-Water Concentration About an Ellipsoid of Fineness Ratio 5 Moving in a Droplet Field," NACA-TN-3153 (July 1954).
5. G. F. Carrier, M. Krook, C. E. Pearson, Functions of a Complex Variable (McGraw-Hill Book Company, 1966). Sec. 2.6.
6. N. A. Fuchs, The Mechanics of Aerosols, Translated by R. E. Daisley and M. Fuchs, edited by C. N. Davies (MacMillan, New York, 1964). Chapter III.
7. C. N. Davies and M. Aylward, "The Trajectories of Heavy, Solid Particles in a Two-Dimensional Jet of Ideal Fluid Impinging Normally upon a Plate," *Proc. Phys. Soc. (London)* B64, 889 (1951).
8. C. N. Davies and C. V. Peetz, "Impingement of Particles on a Transverse Cylinder," *Proc. Roy. Soc. (London)* A234, 269 (1956).
9. K. V. Beard and S. N. Grover, "Numerical Collision Efficiencies for Small Raindrops Colliding with Micron Size Particles," *J. Atmos. Sci.* 31, 543 (1974).
10. R. L. Pitter and H. R. Pruppacher, "A Numerical Investigation of Collision Efficiencies of Simple Ice Plates Colliding with Supercooled Water Drops," *J. Atmos. Sci.* 31, 551 (1974).
11. I. Langmuir and K. B. Blodgett, "Mathematical Investigation of Water Droplet Trajectories," General Electric Company, Report RL-225 (1945).
12. R. G. Dorsch, R. J. Brun, and J. L. Gregg, "Impingement of Water Droplets on an Ellipsoid with Fineness Ratio 5 in Axisymmetric Flow," NACA TN-3099 (March 1954). (Also see NACA TN-2952, 2999, 3047, 3155, 3410, 3153, 3586).

13. H. G. Norment, "Research on Circulation in Nuclear Clouds, II," Technical Operations, Inc., Report TO-B 64-102 (November 1964). AD-361 074.
14. B. Etkin, "Interaction of Precipitation with Complex Flows," Proceedings of the Third International Conference on Wind Effects on Buildings and Structures, (Tokyo, 1971).
15. S. A. Morsi and A. J. Alexander, "An Investigation of Particle Trajectories in Two-Phase Flow Systems," J. Fluid Mech. 55, 193 (1972).
16. S. Kuo-Kai Chai, "Droplet Trajectories Around Aircraft Wing," Thesis, U. Nevada, Reno (November 1973).
17. F. T. Krogh, "Variable Order Integrators for Numerical Solution of Ordinary Differential Equations," Jet Propulsion Lab Technology Utilization Document No. CP-2308 (November 1970).
18. T. E. Hull, W. H. Enright, B. M. Fellen, and A. E. Sedgwick, "Comparing Numerical Methods for Ordinary Differential Equations," SIAM J. Numer. Anal. 9, 603 (1972).
19. J. L. Hess and A. M. O. Smith, "Calculation of Non-Lifting Potential Flow about Arbitrary Three-Dimensional Bodies," McDonnell Douglas Report E. S. 40622 (15 March 1962). AD-282 255.
20. J. L. Hess and A. M. O. Smith, "Calculation of Potential Flow About Arbitrary Bodies," in Progress in Aeronautical Sciences, Vol. 8, edited by D. Kuchemann (Pergamon Press, New York, 1967).
21. F. A. Woodward, "Analysis and Design of Wing-Body Combinations at Subsonic and Supersonic Speeds," J. Aircraft 5, 528 (1968).
22. R. Gunn and G. D. Kinzer, "The Terminal Velocity of Fall for Water Droplets in Stagnant Air," J. Meteor. 6, 243 (1949).
23. K. V. Beard and H. R. Pruppacher, "A Determination of the Terminal Velocity and Drag of Small Water Drops by Means of a Wind Tunnel," J. Atmos. Sci. 26, 1066 (1969).
24. H. R. Pruppacher and K. V. Beard, "A Wind Tunnel Investigation of the Internal Circulation and Shape of Water Drops Falling at Terminal Velocity in Air," Quart. J. Roy. Met. Soc. 96, 247 (1970).
25. H. R. Pruppacher and R. L. Pitter, "A Semi-Empirical Determination of the Shape of Cloud and Rain Drops," J. Atmos. Sci. 28, 86 (1971).
26. C. Magono and C. W. Lee, J. Fac. of Sci., Hokkaido U., Ser. VII, Vol. II, 321 (1966).

27. N. H. Fletcher, The Physics of Rainclouds (Cambridge University Press, 1966).
28. B. J. Mason, The Physics of Clouds (Clarendon Press, Oxford, 1971).
29. A. Ono, "Growth Mode of Ice Crystals in Natural Clouds," J. Atmos. Sci. 27, 649 (1970).
30. A. J. Heymsfield and R. G. Knollenberg, "Properties of Cirrus Generating Cells," J. Atmos. Sci. 29, 1358 (1972).
31. A. H. Auer and D. L. Veal, "The Dimension of Ice Crystals in Natural Clouds," J. Atmos. Sci. 27, 919 (1970).
32. K. O. L. F. Jayaweera and B. F. Ryan, "Terminal Velocities of Ice Crystals," Quart. J. Roy. Met. Soc. 98, 193 (1972).
33. K. O. L. F. Jayaweera and B. J. Mason, "The Behavior of Freely Falling Cylinders and Cones in a Viscous Fluid," J. Fluid Mech. 22, 709 (1965).
34. G. M. Bragg, L. van Zuider, and C. E. Hermance, "The Free-Fall of Cylinders at Intermediate Reynolds Numbers," Atmos. Environ. 8, 755 (1974).
35. K. O. L. F. Jayaweera and B. J. Mason, "The Falling Motions of Loaded Cylinders and Discs Simulating Snow Crystals," Quart. J. Roy. Met. Soc. 92, 151 (1966).
36. J. Zikmunda and G. Vali, "Fall Patterns and Fall Velocities of Rimed Ice Crystals," J. Atmos. Sci. 29, 1334 (1972).
37. R. P. Whitten, "An Investigation of Some Aerodynamic Factors Affecting Meteorological Instrument Readings on a C130A Research Aircraft," Allied Research Associates, AFRD TN-60-454 (15 May 1960).
38. R. D. Ingebo, "Drag Coefficients for Droplets and Solid Spheres in Clouds Accelerating in Airstreams," NACA-TN 3762 (Sept. 1956).
39. T. L. Ogden and K. O. L. F. Jayaweera, "Drag Coefficients of Water Drops Decelerating in Air," Quart. J. Roy. Met. Soc. 97, 571 (1971).
40. C. N. Davies, "Definitive Equations for the Fluid Resistance of Spheres," Proc. Phys. Soc. (London) 57, 259 (1945).
41. M. Kajikawa, "A Model Experimental Study on the Falling Velocity of Ice Crystals," J. Met. Soc. Japan 49, 367 (1971).
42. K. O. L. F. Jayaweera and R. E. Cottis, "Fall Velocities of Plate-Like and Columnar Ice Crystals," Quart. J. Roy. Met. Soc. 95, 703 (1969).